Development of anisotropy in incompressible magnetohydrodynamic turbulence

Barbara Bigot,[1,2] Sébastien Galtier,[1,3] and Hélène Politano[2]
[1]*Institut d'Astrophysique Spatiale, Bâtiment 121, Université Paris-Sud XI, UMR 8617, 91405 Orsay, France*
[2]*Université de Nice–Sophia Anitopolis, CNRS UMR 6202, Obervatoire de la Côte d'Azur, Boîte Postale 42229, 06304 Nice Cedex 4, France*
[3]*Institut Universitaire de France*
(Received 23 April 2008; published 2 December 2008)

We present a set of three-dimensional direct numerical simulations of incompressible decaying magnetohydrodynamic turbulence in which we investigate the influence of an external uniform magnetic field $\mathbf{B_0}$. A parametric study in terms of B_0 intensity is made where, in particular, we distinguish the shear-from the pseudo-Alfvén waves dynamics. The initial kinetic and magnetic energies are equal with a negligible cross correlation. Both the temporal and spectral effects of $\mathbf{B_0}$ are discussed. A subcritical balance is found between the Alfvén and nonlinear times with both a global and a spectral definition. The nonlinear dynamics of strongly magnetized flows is characterized by a different $k_\perp$ spectrum (where $\mathbf{B_0}$ defines the parallel direction) if it is plotted at a fixed $k_\parallel$ (two-dimensional spectrum) or if it is integrated (averaged) over all $k_\parallel$ (one-dimensional spectrum). In the former case a much wider inertial range is found with a steep power law, closer to the wave turbulence prediction than the Kolmogorov one such as in the latter case. It is believed that the averaging effect may be a source of difficulty to detect the transition towards wave turbulence in natural plasmas. Another important result of this paper is the formation of filaments reported within current and vorticity sheets in strongly magnetized flows, which modifies our classical picture of dissipative sheets in conductive flows.

DOI: 10.1103/PhysRevE.78.066301 PACS number(s): 47.27.Jv, 47.65.−d, 52.30.Cv, 95.30.Qd

I. INTRODUCTION

The magnetohydrodynamics (MHD) approximation has proved to be quite successful in the study of a variety of astrophysical plasmas, electrically conducting gas or fluids, such as those found in the solar corona, the interplanetary medium, or in the interstellar clouds. These media are characterized by extremely large Reynolds numbers (up to 10^{13}) [1] with a range of available scales from 10^{18} m to a few meters. The isotropy assumption, usually used in hydrodynamic turbulence, is particularly difficult to justify when dealing with astrophysical flows since a large-scale magnetic field is almost always present such as in the inner interplanetary medium where the magnetic field lines form an Archimedean spiral near the equatorial plane (see, e.g., [2,3]). Thus, MHD turbulence is much more complex than Navier-Stokes turbulence with, in particular, a nonlinear transfer between structures of various sizes due to both nonlinear couplings and Alfvén wave propagation along the background magnetic field.

In the mid 1960s, Iroshnikov [4] and Kraichnan [5] (hereafter IK) proposed a first description of incompressible MHD turbulence. In this approach à la Kolmogorov, the large-scale magnetic field is supposed to act on small scales as a uniform magnetic field, leading to counterpropagating Alfvén waves whose interactions with turbulent motions produce a slowdown of the nonlinear energy cascade. The typical transfer time through the scales is then estimated as τ_{NL}^2/τ_A (instead of τ_{NL} for Navier-Stokes turbulence), where $\tau_{NL}\sim\ell/u_\ell$ is the nonlinear eddy turnover time at characteristic length scale ℓ and u_ℓ is the associated velocity. The Alfvén time is $\tau_A \sim \ell/B_0$, where B_0 represents the large-scale magnetic field normalized to a velocity ($\mathbf{B_0}\rightarrow\mathbf{B_0}\sqrt{\mu_0\rho_0}$, with μ_0 the magnetic permeability of free space and ρ_0 the uniform plasma density). Note that we will use this renormalization in the rest of the paper; hence, the IK energy spectrum in $k^{-3/2}$ unlike the $k^{-5/3}$ Kolmogorov one for neutral flows.

The weakness of the IK phenomenology is the apparent contradiction between the presence of Alfvén waves and the absence of an external uniform magnetic field. The external field is supposed to be played by the large-scale magnetic field, but its main effect, i.e., anisotropy, is not included in the description. The role of a uniform magnetic field has been widely discussed in the literature and, in particular, during the last two decades [6–23]. At strong $\mathbf{B_0}$ intensity, one of the most clearly established results is the bidimensionalization of MHD turbulent flows with a strong reduction of nonlinear transfers along $\mathbf{B_0}$. In the early 1980s, it was shown that a strong B_0 leads to anisotropic turbulence with an energy concentration near the plane $\mathbf{k}\cdot\mathbf{B_0}=0$ [6], a result confirmed later on by direct numerical simulations in two and three space dimensions [7,9]. A linear dependence between anisotropy and $\mathbf{B_0}$ intensity was also suggested [13]. From an observational point of view, we also have evidence that astrophysical (and laboratory) plasmas are mostly in anisotropic states like in the solar wind (see, e.g., [24,25]) or in the interstellar medium (see, e.g., [26]).

The effects of a strong uniform magnetic field may be handled through an analysis of resonant triadic interactions [7] between the wave vectors $(\mathbf{k},\mathbf{p},\mathbf{q})$, which satisfy the relation $\mathbf{k}=\mathbf{p}+\mathbf{q}$, whereas the associated wave frequencies satisfy, for example, $\omega(\mathbf{k})=\omega(\mathbf{p})-\omega(\mathbf{q})$. The Alfvén frequency is $\omega(\mathbf{k})=\mathbf{k}\cdot\mathbf{B_0}=k_\parallel B_0$, where $\parallel$ defines the direction along $\mathbf{B_0}$ ($\perp$ will be the perpendicular direction to $\mathbf{B_0}$). The solution of these three-wave resonant conditions directly gives $q_\parallel=0$, which implies a spectral transfer only in the perpendicular direction. For a strength of B_0 well above the rms level of the kinetic and magnetic fluctuations, the nonlinear interactions of Alfvén waves may dominate the dynamics of the MHD

flow leading to the regime of (weak) wave turbulence where the energy transfer, stemming from three-wave resonant interactions, can only increase the perpendicular component of the wave vectors, while the nonlinear transfer is completely inhibited along $\mathbf{B_0}$ [14,16].

Another important issue discussed in the literature is the relationship between perpendicular and parallel scales in anisotropic MHD turbulence (see [8,10,22]). In order to take into account the anisotropy, Goldreich and Shridar [10] proposed a heuristic model based on a critical balance between linear wave periods and nonlinear turnover time scales, respectively, $\tau_A \sim \ell_\parallel / B_0$ and $\tau_{NL} \sim \ell_\perp / u_\ell$ (where $\ell_\parallel$ and $\ell_\perp$ are the typical length scales parallel and perpendicular to $\mathbf{B_0}$), with $\tau_A = \tau_{NL}$ at all inertial scales. Following the Kolmogorov arguments, one ends up with a $E(k_\perp, k_\parallel) \sim k_\perp^{-5/3}$ energy spectrum [where $\mathbf{k} \equiv (\mathbf{k}_\perp, k_\parallel)$ and $k_\perp \equiv |\mathbf{k}_\perp|$] with the anisotropic scaling law

$$k_\parallel \sim k_\perp^{2/3}. \tag{1}$$

A generalization of this result has been proposed recently [27] in an attempt to model MHD flows in both the weak and strong turbulent regimes, as well as in the transition between them. In this heuristic model, the time-scale ratio $\chi = \tau_A / \tau_{NL}$ is supposed to be constant at all scales but not necessarily equal to unity. The relaxation of this constraint enables one to still recover the anisotropic scaling law (1) and to find a universal prediction for the total energy spectrum $E(k_\perp, k_\parallel) \sim k_\perp^{-\alpha} k_\parallel^{-\beta}$, with $3\alpha + 2\beta = 7$. According to direct numerical simulations (see, e.g., [28–30]), one of the most fundamental results seems to be the anisotropic scaling law between parallel and perpendicular scales (1) and an approximately constant ratio χ, generally smaller than one, between the Alfvén and the nonlinear times. This subcritical value of χ implies therefore a dynamics mainly driven by Alfvén wave interactions.

In the weak turbulence limit, the time-scale separation $\chi \ll 1$, leads to the destruction of some nonlinear terms, including the fourth-order cumulants, and only the resonance terms survive [14,16,31,32], which allows one to obtain a natural asymptotic closure for the wave kinetic equations. In the absence of helicities and for $k_\perp \gg k_\parallel$, the dynamics is then entirely governed by shear-Alfvén waves, the pseudo-Alfvén waves being passively advected by the previous one. In the case of an axisymmetric turbulence, and in the absence of cross correlation between velocity and magnetic field fluctuations, the exact power-law solution is $E(k_\perp, k_\parallel) \sim k_\perp^{-2} f(k_\parallel)$, where f is an arbitrary function taking into account the transfer inhibition along $\mathbf{B_0}$. The regime of wave turbulence is quite difficult to reproduce by direct numerical simulations since it requires a strong external magnetic field as well as a high spatial resolution. According to a recent theoretical analysis, it seems to be currently not possible to fully reach this regime [33] and only the transition towards such a regime is likely to be obtained [23,34].

In order to better understand the development of anisotropy in natural magnetized plasmas, we perform a set of tridimensionnal numerical simulations of incompressible MHD. In this work, the regime of freely decaying flows is chosen in an attempt to model the nonlinear evolution of outward and inward propagating Alfvén waves. We mainly focus our analysis on the development of anisotropy in flows at moderate Reynolds numbers, which freely evolve under the influence of a uniform magnetic field whose strength will be taken as a parameter. The details of the numerical setup and simulations are given in the next section. In Sec. III, we investigate the temporal characteristics of the different flows, as well as different global quantities to measure the spectral anisotropy. Section IV is devoted to the evolution of the energy spectra together with their fluxes. The flow spatial properties are examined in Sec. V. Section VI discusses the second set of simulations. A summary and a conclusion are given in Sec. VII.

II. NUMERICAL SETUP

A. Incompressible MHD equations

The MHD equations that describe the large-scale and low-frequency dynamics of magnetized plasmas are, in the incompressible case and in the presence of a uniform magnetic field $\mathbf{B_0}$,

$$\partial_t \mathbf{v} - B_0 \partial_\parallel \mathbf{b} + \mathbf{v} \cdot \nabla \mathbf{v} = -\nabla P_* + \mathbf{b} \cdot \nabla \mathbf{b} + \nu \Delta \mathbf{v}, \tag{2}$$

$$\partial_t \mathbf{b} - B_0 \partial_\parallel \mathbf{v} + \mathbf{v} \cdot \nabla \mathbf{b} = \mathbf{b} \cdot \nabla \mathbf{v} + \eta \Delta \mathbf{b}, \tag{3}$$

$$\nabla \cdot \mathbf{v} = 0, \tag{4}$$

$$\nabla \cdot \mathbf{b} = 0, \tag{5}$$

where $\mathbf{v}$ is the plasma flow velocity, $\mathbf{b}$ is the magnetic field (normalized to a velocity), P_* is the total (magnetic plus kinetic) pressure, ν is the viscosity, and η is the magnetic diffusivity. It is convenient to introduce the Elsässer fields $\mathbf{z}^\pm = \mathbf{u} \pm \mathbf{b}$ for the fluctuations; in this case and assuming a unit magnetic Prandtl number (i.e., $\nu = \eta$), we get

$$\partial_t \mathbf{z}^\pm + \mathbf{z}^\mp \cdot \nabla \mathbf{z}^\pm \mp B_0 \partial_\parallel \mathbf{z}^\pm = -\nabla P_* + \nu \nabla^2 \mathbf{z}^\pm, \tag{6}$$

$$\nabla \cdot \mathbf{z}^\pm = 0. \tag{7}$$

Note that the second term in the left-hand side (LHS) of Eq. (6) represents the nonlinear interactions between the $\mathbf{z}^\pm$ fields, while the third term represents the linear Alfvénic wave propagation along the $\mathbf{B_0}$ field, which will be assimilated to the z direction in our numerical box. In the present analysis, a unit magnetic Prandtl number is taken in order to extend at maximum the inertial range for both the kinetic and magnetic energies. We believe that such analysis is the first step in understanding turbulence in anisotropic media. The extension to other magnetic Prandtl numbers is the second step: this situation, more realistic for turbulence like in the interstellar medium, is supposed to keep a high level of turbulence for both the kinetic and magnetic energies, which necessitates a higher spatial resolution.

B. Poloidal and toroidal decomposition

In the presence of a large-scale magnetic field $\mathbf{B_0}$, Alfvén waves develop and propagate at Alfvén speed B_0 along the

TABLE I. Computational parameters for runs **Ia–VIIa** with isotropic initial conditions, and for runs **Ib** and **IIb** with specific initial conditions (see the text). Note that simulations **VIIa** and **IIb** use a hyperviscosity and a hyperdiffusivity (dissipation terms in ∇^4). Spatial resolution, viscosity ν $(=\eta)$, and applied magnetic field intensity B_0 are given, followed by initial integral length scales: isotropic $L=2\pi\int[E^v(k)/k]dk/\int E^v(k)dk$, perpendicular $L_\perp=2\pi\int[E^v(k_\perp)/k_\perp]dk_\perp/\int E^v(k_\perp)dk_\perp$, and parallel $L_\parallel=2\pi\int[E^v(k_\parallel)/k_\parallel]dk_\parallel/\int E^v(k_\parallel)dk_\parallel$ scales. Initial rms velocity $u_{rms}=\langle\mathbf{v}^2\rangle^{1/2}$ $(-b_{rms}=\langle\mathbf{b}^2\rangle^{1/2})$ fluctuation is given together with the initial kinetic Reynolds number $\mathcal{R}_v=u_{rms}L/\nu$. Finally, we find typical times: isotropic eddy turnover time $\tau^i_{NL}=L/u_{rms}$ (based on the isotropic length scale L), eddy turnover time $\tau_{NL}=L_\perp/u_{rms}$ (based on $L_\perp$), Alfvén time based on rms magnetic fluctuations $\tau^i_A=L/b_{rms}$, Alfvén wave period $\tau_A=L_\parallel/B_0$, and the final time t_M of the numerical simulation.

		ν	B_0	L	$L_\perp$	$L_\parallel$	u_{rms}	$\mathcal{R}_v$	τ^i_{NL}	τ_{NL}	τ^i_A	τ_A	t_M
Ia	256^3	4.10^{-3}	0	3.12			1	779	3.12		3.12		15
IIa	256^3	4.10^{-3}	1	3.12	3.85	5.57	1	779	3.12	3.85	3.12	5.57	15
IIIa	256^3	4.10^{-3}	5	3.12	3.85	5.57	1	779	3.12	3.85	3.12	1.11	15
IVa	256^3	4.10^{-3}	15	3.12	3.85	5.57	1	779	3.12	3.85	3.12	0.37	15
Va	$512^2\times64$	10^{-3}	15	3.12	3.85	5.57	1	3120	3.12	3.85	3.12	0.37	15
VIa	$512^2\times64$	10^{-3}	30	3.12	3.85	5.57	1	3120	3.12	3.85	3.12	0.18	15
VIIa	$512^2\times64$	10^{-6}	15	3.12	3.85	5.57	1	3.12×10^6	3.12	3.85	3.12	0.37	15
Ib	$512^2\times64$	5.10^{-4}	15	1.27	1.90	2.04	1	2530	1.26	1.90	1.26	0.13	40
IIb	$512^2\times64$	10^{-6}	15	1.27	1.90	2.04	1	3.16×10^6	1.26	1.90	1.26	0.13	40

$\mathbf{B_0}$ direction. These waves may be decomposed into shear- and pseudo-Alfvén waves denoted, respectively, $\mathbf{z}_1^\pm$ and $\mathbf{z}_2^\pm$. The divergence-free condition implies that only two types of scalar field ($\psi^\pm$ and $\phi^\pm$) are needed to describe the incompressible MHD dynamics which are, respectively, the toroidal and poloidal fields. For the Fourier transforms of the involved fields, we have:

$$\hat{\mathbf{z}}^\pm(\mathbf{k})=\hat{\mathbf{z}}_1^\pm(\mathbf{k})+\hat{\mathbf{z}}_2^\pm(\mathbf{k}), \tag{8}$$

with

$$\hat{\mathbf{z}}_1^\pm(\mathbf{k})=i\mathbf{k}\times\mathbf{e}_\parallel\hat{\psi}^\pm(\mathbf{k}), \tag{9}$$

$$\hat{\mathbf{z}}_2^\pm(\mathbf{k})=-\frac{\mathbf{k}\times(\mathbf{k}\times\mathbf{e}_\parallel)}{k}\hat{\phi}^\pm(\mathbf{k}), \tag{10}$$

where in our simulations $k_\perp=\sqrt{k_x^2+k_y^2}$ and $k=\sqrt{k_x^2+k_y^2+k_z^2}$. Here, $k_z\equiv k_\parallel$ and $\mathbf{e}_\parallel$ denotes the unit vector parallel to the $\mathbf{B_0}$ direction. Hence, the shear-Alfvén waves correspond to a vector field perpendicular to the external magnetic field $\mathbf{B_0}$, whereas the pseudo-Alfvén waves is a vector field which may have a component along $\mathbf{B_0}$; but both vector fields depend on the three coordinates of $\mathbf{k}$.

C. Initial conditions

We numerically integrate the three-dimensional incompressible MHD equations (2)–(5), in a 2π-periodic box, using a pseudospectral code (including dealiasing), and with spatial resolution from 256^3 to $512^2\times64$ grid points according to the initial conditions (see Table I). The time marching uses an Adams-Bashforth or Cranck-Nicholson scheme, i.e., a second-order finite-difference scheme in time (see, e.g., [35]).

1. Runs Ia to IVa

The initial kinetic and magnetic fluctuations are characterized by spectra at large scales, i.e., for $k=[1,8]$, proportional to $k^2\exp(-k^2/4)$; for $k>8$, the spectra are exactly equal to zero. This condition means that for wave numbers k up to 2, we have mainly a flat modal spectrum, which prevents initially any favored wave vectors. No forcing is present during the simulations and the flows may evolve freely for time $t>0$. The associated kinetic,

$$E^v=\frac{1}{2}\langle\mathbf{u}^2(\mathbf{x})\rangle, \tag{11}$$

and magnetic,

$$E^b=\frac{1}{2}\langle\mathbf{b}^2(\mathbf{x})\rangle, \tag{12}$$

energies are chosen initially equal, namely, $E^v(t=0)=E^b(t=0)=0.5$. (Note that $\langle\cdot\rangle$ means space averaging.)

The correlation between the velocity and magnetic-field fluctuations, which is measured by the cross correlation

$$\rho\equiv\frac{2\langle\mathbf{u}(\mathbf{x})\cdot\mathbf{b}(\mathbf{x})\rangle}{\langle\mathbf{u}^2(\mathbf{x})+\mathbf{b}^2(\mathbf{x})\rangle}, \tag{13}$$

is initially less than 1%.

The initial (large-scale) kinetic and magnetic Reynolds numbers are about 800 for the flows with $\nu=4\times10^{-3}$ (see Table I), with $u_{rms}=b_{rms}=1$; the isotropic integral scale is

$$L=2\pi\frac{\int[E^v(k)/k]dk}{\int E^v(k)dk}\sim\pi. \tag{14}$$

A parametric study is performed according to the intensity of B_0. Four different values are used, namely, $B_0=0$, 1, 5, and 15. All these simulations are run up to a maximum computational time $t_M=15$, and correspond to runs **Ia** to **IVa** described in Table I.

2. Runs Va to VIIa

Taking advantage of the strong reduction of the nonlinear transfers along $\mathbf{B_0}$ in highly magnetized flows, a second set of direct numerical simulations is performed with a spatial resolution of 512^2 grid points in the perpendicular plane to $\mathbf{B_0}$ and with only 64 grid points in the parallel direction (runs **Va** and **VIa** in Table I). For such runs, the initial conditions are the same as before with, however, a uniform magnetic field $B_0=15$ and 30, and a smaller viscosity.

Such simulations were analyzed in the past to explore the self-consistency of the reduced MHD model [36] with the conclusion that small values of viscosities, adjusted according to the transverse dynamics, are not incompatible with the smaller spatial resolution in the parallel direction since the transfer toward small scales is also reduced along the uniform magnetic field. We checked that the viscosity $\nu=10^{-3}$ is indeed well adjusted. Note that such a small aspect ratio may reduce the number of resonant wave interactions, which in turn may affect the dynamics (see, e.g., [37]). However, in Alfvén wave turbulence, the resonant manifolds foliate wave-vector space [14] which, in principle, prevents such a problem.

In the same manner, another computation (run **VIIa**) is made using a hyperviscous scheme, where the Laplacian operator of the dissipative terms is replaced by a bi-Laplacian, in order to enlarge the inertial range of the energy spectra.

3. Runs Ib and IIb

Finally, to evaluate the influence of the initial conditions, a third set of runs is performed with a uniform magnetic field fixed to $B_0=15$, and with either a viscous (**Ib**) or a hyperviscous dissipation (**IIb**). In both simulations, we use $512^2 \times 64$ grid points. The specific initial conditions of these runs correspond to a modal energy spectrum $E^{\pm}(k_\perp,k_\parallel) = C(k_\parallel)k_\perp^3$, for $k_\perp$ and $k_\parallel \in [0,4]$, the value of $C(k_\parallel)$ increasing with $k_\parallel$ to reach a maximum at $k_\parallel=4$. Note that this initial spectrum allows a transient period of cascade toward smaller scales during which energy is mainly conserved. Initially, the ratio between kinetic and magnetic energies is still fixed to 1, whereas the cross-correlation coefficient is zero. A first set of results was given in [23].

For all the runs described in this section, the computational parameters (initial Reynolds numbers, characteristic length scales and times…) are summarized in Table I.

III. TEMPORAL ANALYSIS

A. Energetic properties

1. Elsässer $\mathbf{z}^{\pm}$ Cartesian fields

In this section, we study the temporal behavior of several global quantities to characterize the MHD flow dynamics and the influence of the $\mathbf{B_0}$ strength on it. In all the following figures, time evolutions are shown from initial isotropic conditions up to time t_M (the maximum computational time reached), for simulations **Ia–IVa** at moderate resolution (256^3 mesh points) and $B_0=0$, 1, 5, and 15, together with highly magnetized flows **Va** and **VIa** at $B_0=15$ and 30, using $512^2 \times 64$ spatial resolution (see Table I).

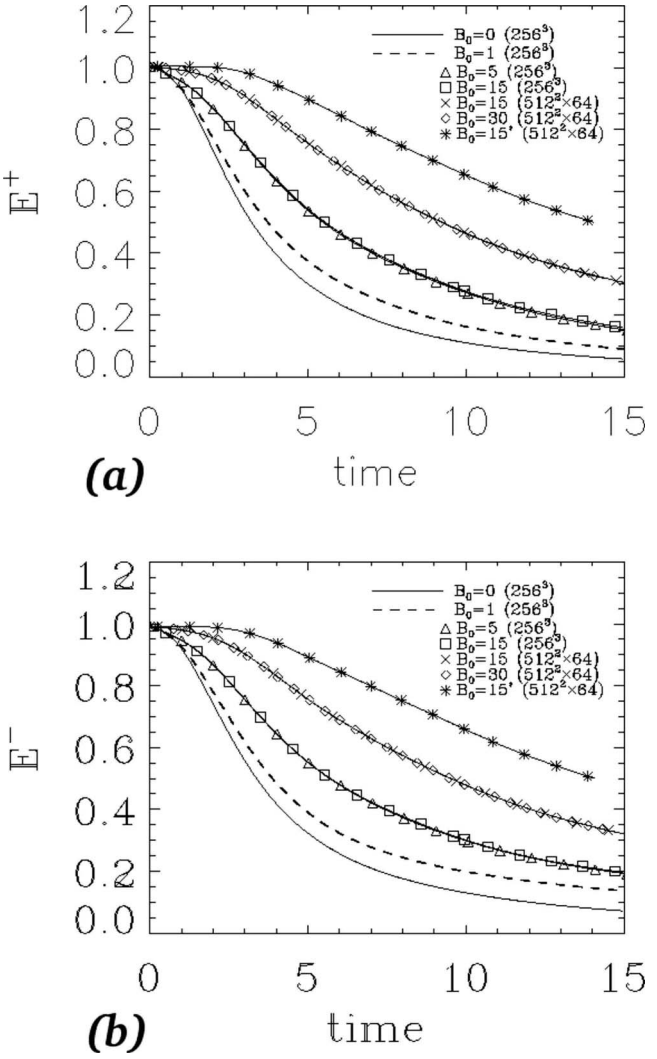

FIG. 1. Temporal evolution of energies E^+ (a) and E^- (b) for $B_0=0,1,5,15$ (runs **Ia–IVa**; 256^3) and $B_0=15,30$ (runs **Va** and **VIa**; $512^2 \times 64$). The hyperviscous run **VIIa** with $B_0=15$ ($512^2 \times 64$) is also given up to $t=14$.

We first consider the evolution of the Elsässer energies,

$$E^{\pm}(t) = \frac{1}{2}\langle \mathbf{z}^{\pm 2}(\mathbf{x})\rangle(t), \tag{15}$$

displayed in Fig. 1. Note that, for periodic boundary conditions, these energies are two independent invariants of the inviscid MHD equations (6), with or without the presence of a uniform magnetic field. Energies $E^+(t)$ and $E^-(t)$ present a similar behavior for a given B_0. For runs **Ia–IIIa**, where $\mathbf{B_0}$ intensity is increased, we clearly see a slowdown of the energy decay. On one hand, this slowing down reflects the energy transfer inhibition along the $\mathbf{B_0}$ direction, and thus, the flow inability to create, in the parallel direction, smaller and smaller scales up to the dissipative ones. Hence, the energy dissipation mainly takes place in transverse planes, which are led to play a more efficient role as the flow magnetization is increased. On the other hand, energy transfers themselves could also be weakened (in the transverse planes) since the

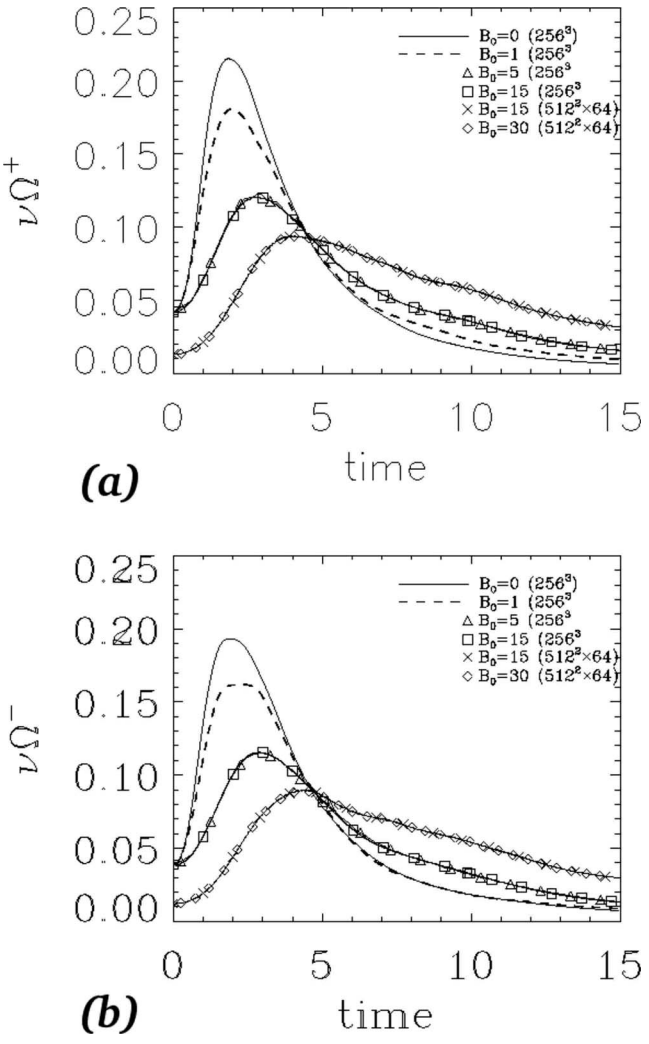

FIG. 2. Temporal evolution of the global dissipation $\nu\Omega^+$ (a) and $\nu\Omega^-$ (b); same viscous runs as in Fig. 1.

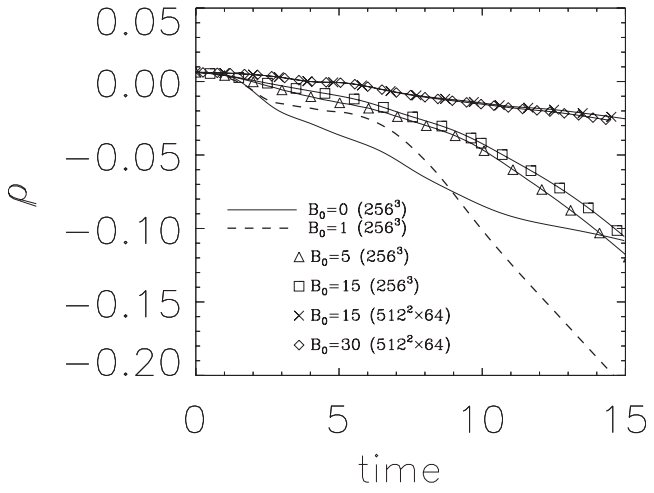

FIG. 3. Temporal evolution of the cross-correlation coefficient ρ; same runs as in Fig. 1.

MHD cascade of energy to smaller scales is produced by successive interactions of oppositely directed waves. Indeed, for higher $\mathbf{B_0}$ intensities, the waves become faster and thus the time duration of an individual collision of $z^{\pm}$ waves decreases. Therefore it takes many more collisions between (fast) Alfvén wave packets (as measured by the ratio between the nonlinear turnover time on the linear wave period; τ_{NL}/τ_A) to have an efficient energy cascade process. One could also note that, for a given flow, a saturation effect occurs according to B_0 intensities. Indeed, the $E^{\pm}(t)$ evolutions are quite similar for flows at $\nu=4\times10^{-3}$ with $B_0=5$ and 15 (runs **IIa** and **IVa**, respectively), as well as for flows at $\nu=10^{-3}$ with $B_0=15$ and 30 (runs **Va** and **VIa**, respectively). The hyperviscous run **VIIa** is also shown but only up to $t=14$. We see that the initial plateau is wider and almost flat because of the larger inertial range and the higher Reynolds number. Then, we see a decay of energy, which is slower than for the other viscous runs.

The B_0 saturation effect is also visible on the time evolution of the global dissipation of the flow,

$$\nu\Omega^{\pm}(t) = \nu\langle[\boldsymbol{\nabla}\times\mathbf{z}^{\pm}]^2(\mathbf{x})\rangle(t), \tag{16}$$

displayed in Fig. 2. The early time dynamics, near the first inflection point, is almost inviscid; it corresponds to the small-scale generation (e.g., at times $t\leqslant 1$ in the $B_0=0$ simulation). As the $\mathbf{B_0}$ intensity is increased, this small-scale development is slightly retarded, which means that the duration of the essentially inviscid phase increases. Moreover, the maximum of the dissipation is substantially reduced, and occurs at later times, namely, $t\sim 2$ for flows with $B_0=0$ and 1, $t\sim 3$ with $B_0=5,15$ and $t\sim 4$ for the less viscous flows with $B_0=15,30$. Altogether, in physical space, this corresponds to the creation of more elongated structures along $\mathbf{B_0}$ as the flow is more magnetized, with a smaller dissipation on the whole, and, in spectral space, to higher inhibition of parallel energy transfers, as already explained. One can also note that the dissipation peak is smoothed in the less viscous flows ($\nu=10^{-3}$), meaning an almost constant dissipation between $t\sim 3$ and $t\sim 5$ in runs **Va** and **VIa** with a more extended range of small scales. Finally, note a different evolution between case **IVa** (with $\nu=4\times10^{-3}$) and **Va** (with $\nu=10^{-3}$) whereas the uniform field B_0 is the same. A factor 4 of difference is visible initially, which may be attributed mainly to a decrease of factor 4 of the viscosity. In this case, the time delay to reach the maximum may be explained by a wider inertial range in $k_{\perp}$ and therefore a longer time needed to reach the dissipative scales (an effect also seen in Fig. 1 with a wider initial plateau where energy is roughly conserved).

Figure 3 shows the cross-correlation coefficient (13) between velocity and magnetic fields, which also reads, in terms of the Elsässer energies, as

$$\rho(t) = \frac{E^+(t) - E^-(t)}{E^+(t) + E^-(t)}. \tag{17}$$

It measures the relative amount of the two $z^{\pm}$ species. Indeed, $\rho(t)\to\pm 1$ means that $E^{\mp}=0$, and hence only one type of wave is excited, whereas when $\rho(t)\to 0$, there are as many z^+ as z^- counterpropagating waves, with the same amount of energy. Initially, $\rho(t=0)\sim 0$ (i.e., less than 1%), and stays so during the flow inviscid phases. Close to the times at which the maximum of dissipation occurs in the different flows,

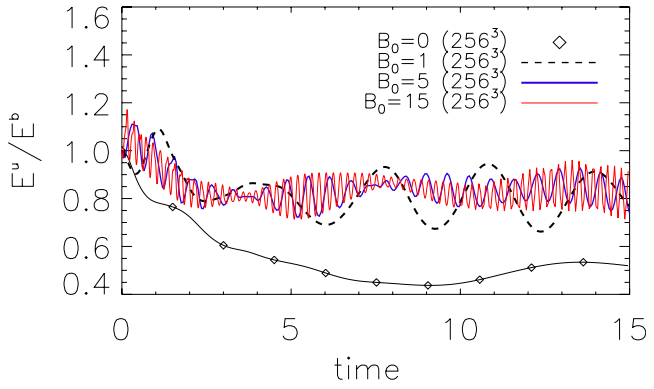

FIG. 4. (Color online) Time evolution of the Alfvén ratio r_A for runs **Ia–IVa**, with $B_0=0$, diamond symbols; $B_0=1$, black dashed line; $B_0=5$, blue (thick dark gray) solid line; and $B_0=15$, the red (thin gray) solid line.

$\rho(t)$ deviates from zero with a lesser departure as the flow is more magnetized, from $B_0=1$ up to $B_0=30$, because the field lines are rigidified by the ambient magnetic field, and the dissipation is delayed. In the case of $B_0=0$, the temporal evolution of the cross-correlation coefficient is globally different, due to the absence of a guiding magnetic field and different dissipative processes. Note, however, that all flows evolve toward an excess of E^- energy.

Apart from this, the prevalence of the Alfvén wave fluctuations can be measured by the so-called Alfvén ratio

$$r_A(t) = \frac{E^v(t)}{E^b(t)} = \frac{\langle \mathbf{v}^2 \rangle(t)}{\langle \mathbf{b}^2 \rangle(t)}, \tag{18}$$

between kinetic and magnetic energies. For example, in the wave turbulence regime we have an equipartition (at the level of the kinematics [14]) between kinetic and magnetic energies. Its departure from unity suggests the presence of non-Alfvénic fluctuations. Indeed, the energy of an individual Alfvén wave is equipartitioned between its kinetic and magnetic components, averaged over a wave period, with thus a ratio $r_A=1$. In the presence of an external magnetic field, exchanges between magnetic and velocity fluctuations, due to Alfvén waves, produce oscillations as shown on $r_A(t)$ in Fig. 4. The period of these oscillations is given by the Alfvén time $\tau_A \sim 5$, 1, and 0.4 (see Table I), which are found by a simple analysis based on the values $B_0=1$, 5, and 15, respectively, and the values of the characteristic parallel length scale $L^{\parallel} \sim 5.57$ for runs **IIa–IVa**. Although initially the magnetic and kinetic energies are chosen equal, $E^v(t=0) = E^b(t=0) = 0.5$, the magnetic energy stabilizes around twice the kinetic energy, after $t \sim 5$, for the nonmagnetized flow ($B_0=0$), while for the magnetized flows, whatever the $\mathbf{B_0}$ intensity is, the magnetic energy saturates to about 1.25 lower than the kinetic energy level after time $t \sim 2$. This result may be compared with solar wind data where the same tendency is found with a domination of the magnetic energy. (This comparison is, however, not direct since outward propagating Alfvén waves are initially dominant.) This Alfvén ratio seems to find a limit of about 1/2 at several astronomical units, which might be explained by the decreasing importance of the large-scale magnetic field at larger heliocentric distances (see e.g., [38]).

Figure 5 displays the probability distribution function (PDF) of the cross correlation for different times (the same runs as in Fig. 3). As expected, we start initially with a distribution clearly centered around zero. As the time increases, we see a distribution shifted towards negative values to finally be centered around −0.4 for the nonmagnetic case. The case $B_0=1$ is even more shifted with a maximum of the distribution around −0.6. The strongly magnetic cases are mainly characterized by the formation of extended plateaus centered around the negative values. This result means that although the cross-correlation coefficient (13) is close to zero for strongly magnetized flows (see Fig. 3), a wide range of values is often reached locally.

2. Shear- and pseudo-Alfvén wave decomposition

In the presence of an external magnetic field, it is convenient to describe the flow dynamics in terms of shear- and pseudo-Alfvén waves, or in other words to use, respectively, the toroidal and poloidal components of the $\mathbf{z}^{\pm}$ fields [see Eq. (8)]. Indeed, the Alfvén waves dynamics for the stronger magnetized flows have crucial consequences on the turbulent properties. We will use here the shear- and pseudo-Alfvén wave decomposition to analyze our numerical simulations and, therefore, we will not consider the $B_0=0$ case anymore.

In Fig. 6, we show the temporal evolutions of energies E_1^+ and E_2^+ associated, respectively, to the shear-Alfvén and pseudo-Alfvén waves; they are defined as

$$E_{1,2}^+(t) = \langle \mathbf{z}_{1,2}^{+2} \rangle(t), \tag{19}$$

and are not inviscid invariants. Note that $E^{\pm} \neq E_1^{\pm} + E_2^{\pm}$ because the energy contained in the $k_{\perp}=0$ modes is not included in the toroidal and poloidal decomposition (although it is, of course, in the original Cartesian fields). First, we observe a slowdown of the energy decay when the intensity of B_0 increases. It is a behavior similar to the one found in Fig. 1 for the energies $E^{\pm}$. With such a decomposition, a similar behavior is also found for runs **IIIa** and **IVa**, and runs **Va** and **VIa**. The important new information is about the initial increase of energies, which is more pronounced for runs **Va** and **VIa**, and for the shear-Alfvén waves. These energies are, in fact, pumped from the $k_{\perp}=0$ mode (the total energy is not an increasing function). Note that the same behavior is found for the − polarity.

Figures 7 present the temporal evolution of the dissipations

$$\nu \Omega_{1,2}^+(t) = \nu \langle [\boldsymbol{\nabla} \times (\mathbf{z}_{1,2}^+)]^2 \rangle(t), \tag{20}$$

for, respectively, the shear- and pseudo-Alfvén waves (only the + polarity is shown since the same behavior is found for the − polarity). No clear difference is found between the type of dissipation. We also note no significant difference with Fig. 2 except a factor of 2 in magnitude because here we do not see the total dissipation for a given polarity but either the shear- or the pseudo-Alfvén waves contribution.

Figure 8 presents the temporal evolution of the Alfvénicity (or Alfvén ratio)

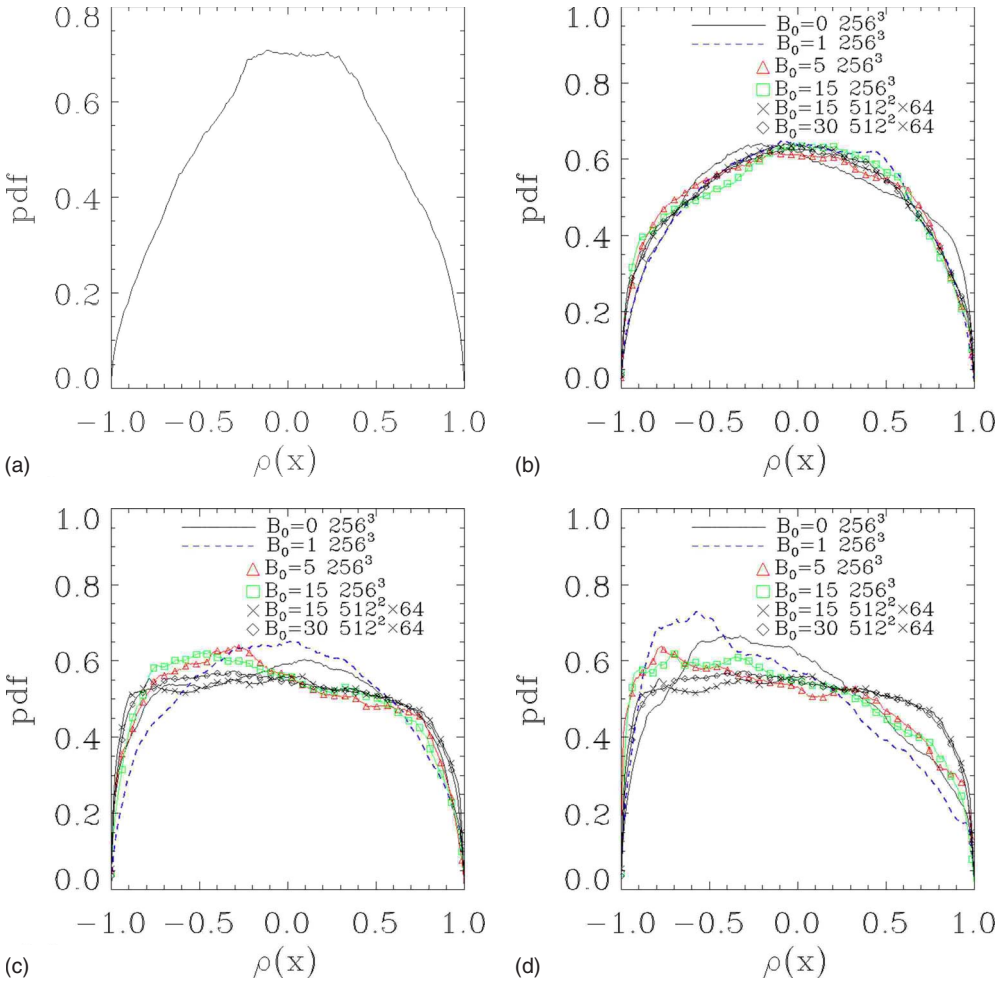

FIG. 5. (Color online) Probability distribution functions of the cross correlation (runs **Ia**–**VIa**) initially (a), at the maximum of the global dissipation (b), when 77% of the total energy is dissipated (c), and at the final time (d).

$$r_{A_{1,2}}(t) = \frac{E^v_{1,2}(t)}{E^b_{1,2}(t)}, \tag{21}$$

for the shear- and pseudo-Afvén waves, respectively, with

$$E^v_{1,2} = \frac{1}{2}\langle (\mathbf{z}^+_{1,2} + \mathbf{z}^-_{1,2})^2 \rangle, \tag{22}$$

and

$$E^b_{1,2} = \frac{1}{2}\langle (\mathbf{z}^+_{1,2} - \mathbf{z}^-_{1,2})^2 \rangle. \tag{23}$$

This plot is particularly interesting since it shows that shear-Alfvén waves and pseudo-Alfvén waves behave differently with an Alfvén ratio of about 1 for the latter and significantly smaller than 1 for the former. Since for strongly magnetized flows the perpendicular fluctuations are mainly made of shear-Alfvén waves and the parallel ones made of pseudo-Alfvén waves, we have here a prediction that can be compared with measurements made in natural plasmas like in the solar wind. Additionally, we observe the same oscillations as in Fig. 4 where the same type of analysis on the time scales may be made.

Figure 9 displays the temporal evolution of the spectral Alfvénicity for shear-Alfvén waves

$$r_{A_1}(k_\parallel, t) = \frac{E^u_1(k_\parallel, t)}{E^b_1(k_\parallel, t)}, \tag{24}$$

with $k_\parallel = 0$, 1, 2, and 3 (run **IIa**–**IVa**). The initial Afvén ratio is close to unity for every parallel wave number, then a different behavior is found for the 2D state ($k_\parallel = 0$), which deviates strongly from the equipartition and tends approximately to 1/2 independently of the B_0 intensity. For the 3D modes, the spectral Alfvén ratio oscillates around unity meaning a tendency towards equipartition between the kinetic and magnetic energies. This tendency is stronger for stronger magnetized flows. Thus the 3D modes follow the dynamics expected in wave turbulence in which an exact equipartition happens [14]. It is actually the 2D state that explains the behavior found previously in Fig. 8, where a discrepancy from the equipartition was observed. Therefore, Fig. 8 is not in contradiction with the wave turbulence regime and offers another possible interpretation of observations in natural plasmas like the solar wind. Note that the

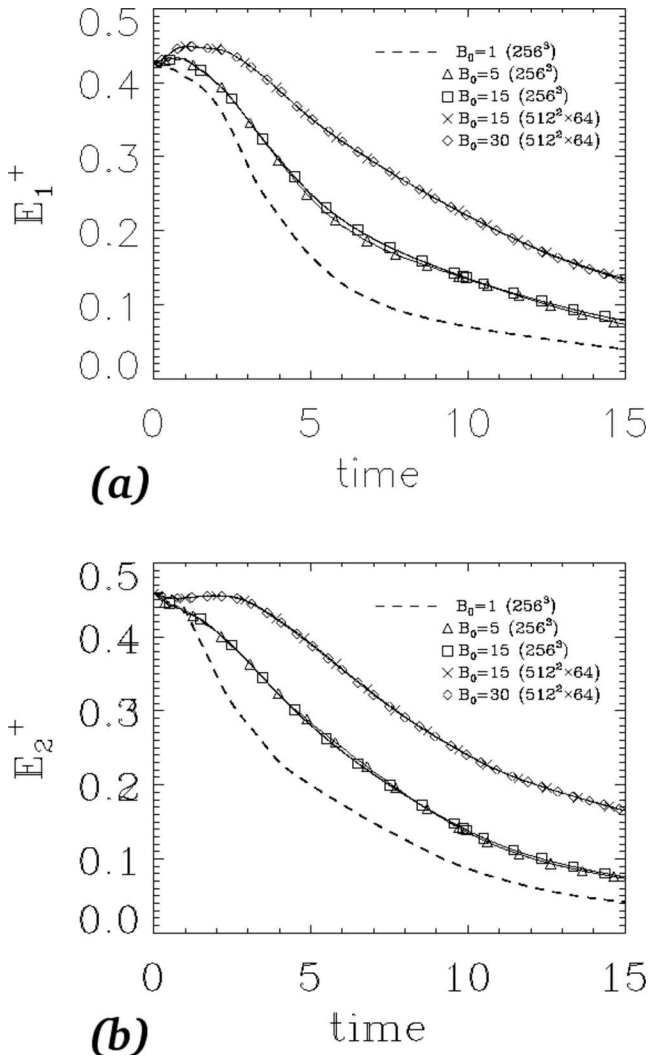

FIG. 6. Temporal evolution of energies (a) E_1^+ and (b) E_2^+ of the shear- and pseudo-Alfvén waves for runs **IIa**–**VIa**.

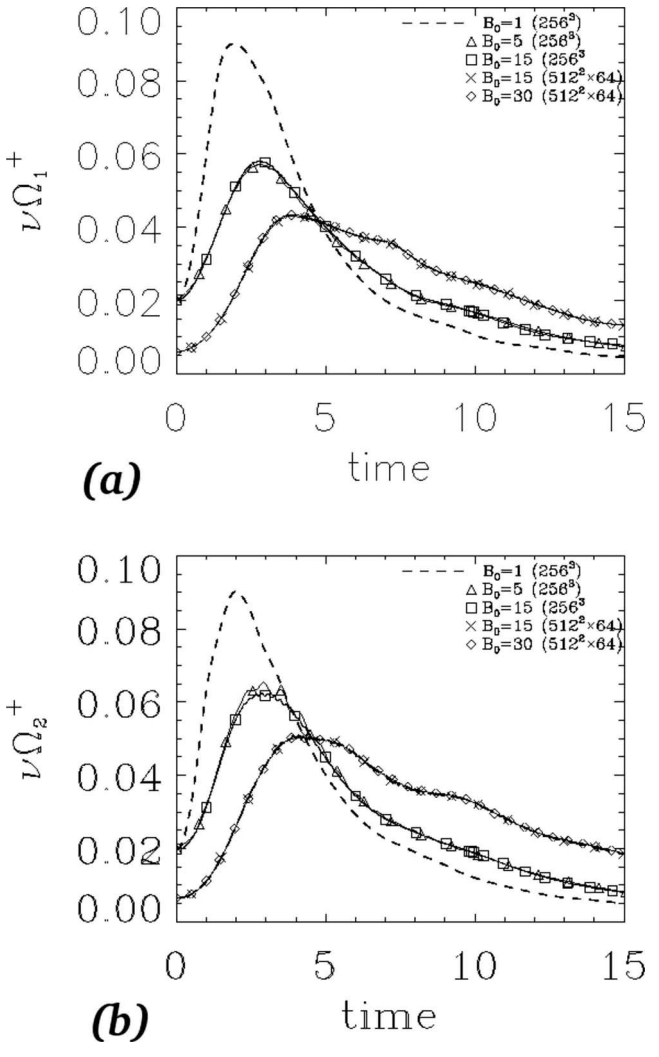

FIG. 7. Temporal evolution of the dissipations (a) $\nu\Omega_1^+$ and (b) $\nu\Omega_2^+$ of shear- and pseudo-Alfvén waves for runs **IIa**–**VIa**.

same type of results are found for pseudo-Alfvén waves (not shown) with a deviation from the equipartition for the 2D state.

B. Characteristic length and time scales

Figures 10 and 11 present the time evolutions of the perpendicular integral length scales, defined as

$$L^+_{\perp_{1,2}} = \frac{\int E^+_{1,2}(k_\perp,k_\parallel)/k_\perp dk_\perp dk_\parallel}{E^+_{1,2}}, \tag{25}$$

and the parallel integral length scales

$$L^+_{\parallel_{1,2}} = \frac{\int E^+_{1,2}(k_\perp,k_\parallel)/k_\parallel dk_\perp dk_\parallel}{E^+_{1,2}}, \tag{26}$$

for, respectively, the shear- and pseudo-Afvén waves. We first note, for shear-Alfvén waves, a decrease of the perpendicular scales and an increase of the parallel one after we observe a saturation. These behaviors may be interpreted as a direct cascade in the perpendicular direction and a possible inverse cascade in the parallel one. The saturation phase with length scales approximately frozen means that the spectra are well developed. The case $B_0=1$ deviates from this analysis because the mean field is not strong enough to impose a full anisotropic dynamics; it can be compared with a previous study made for pure isotropic turbulence [35]. For pseudo-Alfvén waves, the situation is less clear even if we still observe globally the same behavior as before in the initial phase. It is the saturation phase that is the most different with an apparent oscillation that can be related to the period found from the previous analysis made for Fig. 4.

Figure 12 presents the temporal evolution of the nonlinear time

$$\tau^+_{NL_{1,2}} = \frac{L^+_{\perp_{1,2}}}{z^-_{rms_{1,2}}}, \tag{27}$$

and the Alfvén time

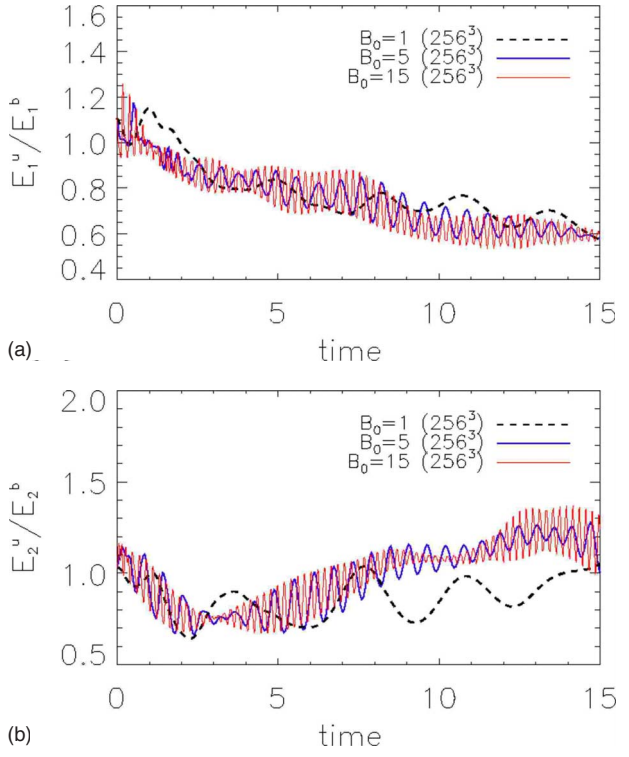

FIG. 8. (Color online) Temporal evolution of the Alfvén ratio for (a) shear- and (b) pseudo-Alfvén waves (runs **IIa**–**IVa**) with $B_0=1$, black dashed line; $B_0=5$ blue (thick dark gray) solid line; and $B_0=15$, red (thin gray) solid line.

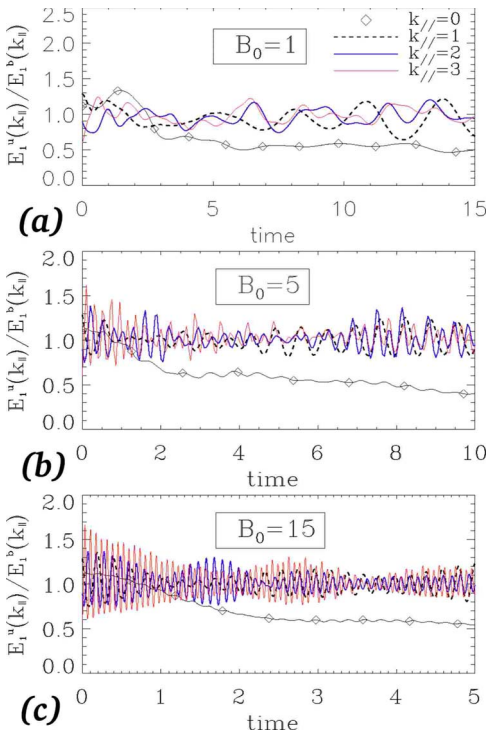

FIG. 9. (Color online) Temporal evolution of the spectral Alfvén ratio for shear-Alfvén waves (runs **IIa**–**IVa**) for (a) $B_0=1$, (b) $B_0=5$, and (c) $B_0=15$ at a given parallel wave number with $k_\parallel=0$, diamond symbols; $k_\parallel=1$, dashed black line; $k_\parallel=2$, blue (thick dark gray) solid line; and $k_\parallel=3$, red (thin gray) solid line.

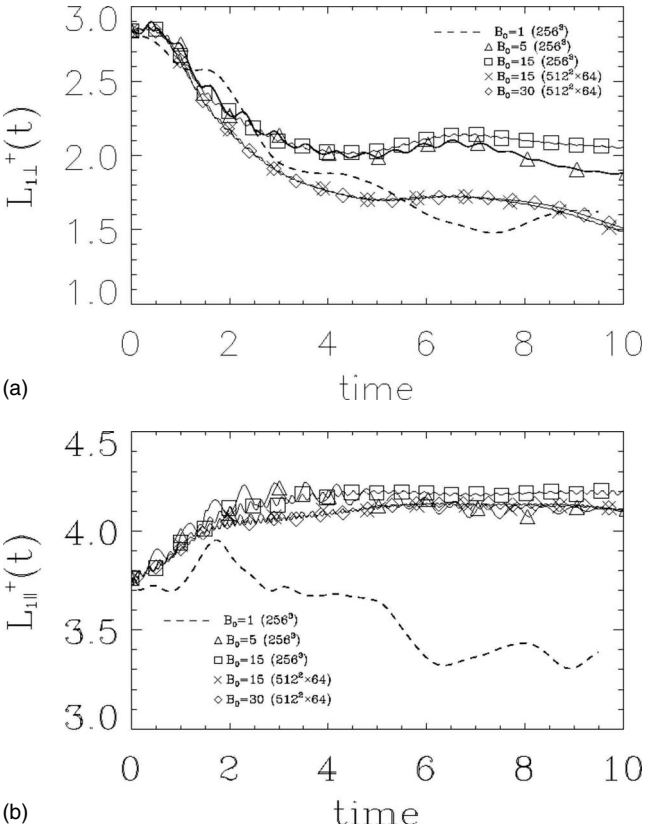

FIG. 10. Temporal evolution, up to $t=10$, of perpendicular (a) and parallel (b) integral length scales for shear-Alfvén (+) waves; same runs as in Fig. 7.

$$\tau^+_{A_{1,2}} = \frac{L^+_{\parallel_{1,2}}}{B_0}, \tag{28}$$

based on the shear- and pseudo-Afvén waves dynamics. We mainly observe a decrease of the Alfvén time when the strength of the uniform field B_0 increases, whereas the nonlinear time is not strongly affected. Note that the profiles of the nonlinear times for the case $B_0=5$ and $B_0=10$ look similar with oscillations whose periods are approximately the same as before. This is simply due to the definition used to build the nonlinear time, which includes the previous length scales. It is also this definition that explains the initial decrease ($t\leqslant 2$) of the nonlinear time since the perpendicular integral length scales follow the same behavior.

Figure 13 shows the temporal evolution (a) of the time-scales ratio

$$\chi^+_1(t) = \frac{\tau^+_{A_1}(t)}{\tau^+_{NL_1}(t)}, \tag{29}$$

between the Alfvén (28) and eddy turnover (27) times. Only the case of shear-Alfvén waves is shown since the same behavior is found for pseudo-Alfvén waves. This new plot gives a quantitative estimate of the balance between the time scales that we discussed in the Introduction. We clearly see that the balance is subcritical [$\chi^+_1(t)$ stays well below unity] as the strength of B_0 increases with a value that remains about constant during the time of the simulation.

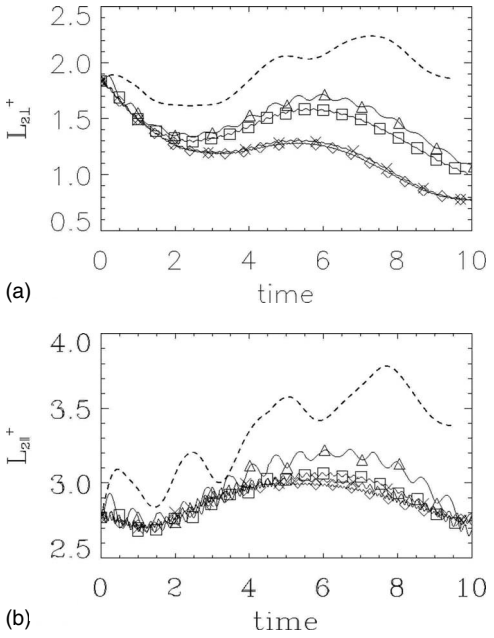

FIG. 11. Temporal evolution, up to $t=10$, of perpendicular (a) and parallel (b) integral length scales for pseudo-Alfvén (+) waves; same runs and legend as in Fig. 10.

Figure 13 also displays the spectral ratio between the Alfvén and nonlinear time scales for shear-Alfvén waves. It is defined as

$$\chi_1^+(k_\perp,k_\parallel)(t)=\frac{k_\perp z_{\ell_1}^-(t)}{k_\parallel B_0}, \tag{30}$$

with

$$z_{\ell_1}^-(t)=\sqrt{E_1^-(k_\perp,k_\parallel)k_\perp k_\parallel}. \tag{31}$$

The previous definition (29) is based on a global estimate of the time scales. This new definition is more precise since it allows one to take into account the scale at which the times are defined. Then, each time evolution is associated with a couple of (spectral) scales $(k_\perp,k_\parallel)$. Different couples have been tried and only those for which the ratio $\chi_1^+(k_\perp,k_\parallel)$ displays an extended plateau have been reported. It is basically for times between $t=2$ and $t=4$, a range of time during which the small scales have been produced and the nonlinear interactions are still important. Note that we still observe oscillations that can be explained in terms of Alfvén time scales.

In Fig. 14, we report each couple $(k_\perp,k_\parallel)$ and show the anisotropic scaling law $k_\parallel \sim k_\perp^{2/3}$ as a reference. We see that such a law well fits the points, which means that the subcritical balance [observe again here with $\chi_1^+(k_\perp,k_\parallel)<1$] is still well described by the anisotropic scaling law (1). This property may be understood by a heuristic model [27] where the time-scale ratio χ is supposed to be constant at all scales but not necessarily equal to unity, which allows one to use the IK phenomenology instead of the Kolmogorov one [10]. [Note that the same behavior is found when $\chi_1^-(k_\perp,k_\parallel)$ is considered.]

The question of the validity of the anisotropic scaling law $k_\parallel \sim k_\perp^{2/3}/B_0$ (we use here the formulation given in [27], which includes the uniform magnetic field) beyond the inertial range, and, in particular, at larger scales, may be addressed from these numerical simulations. A first answer is given in Fig. 14 with the couple $(k_\perp=4,k_\parallel=1)$, which is at the largest scales of the system but does not follow the anisotropic law.

C. Generalized anisotropy angles

To quantify the degree of anisotropy associated with the flow, we use the generalized Shebalin angles (see [7,9], and references therein), defined as

$$\tan^2\theta_{\mathbf{q}}=\frac{\sum k_\perp^2|\mathbf{q}(\mathbf{k},t)|^2}{\sum k_\parallel^2|\mathbf{q}(\mathbf{k},t)|^2}, \tag{32}$$

where $\mathbf{q}$ is a vector field, like $\mathbf{v}$, $\mathbf{b}$, or $\mathbf{z}^\pm$ in Fig. 15. We start initially with a 3D isotropic flow for which $\theta_{\mathbf{q}}\sim 54,74°$. Fig-

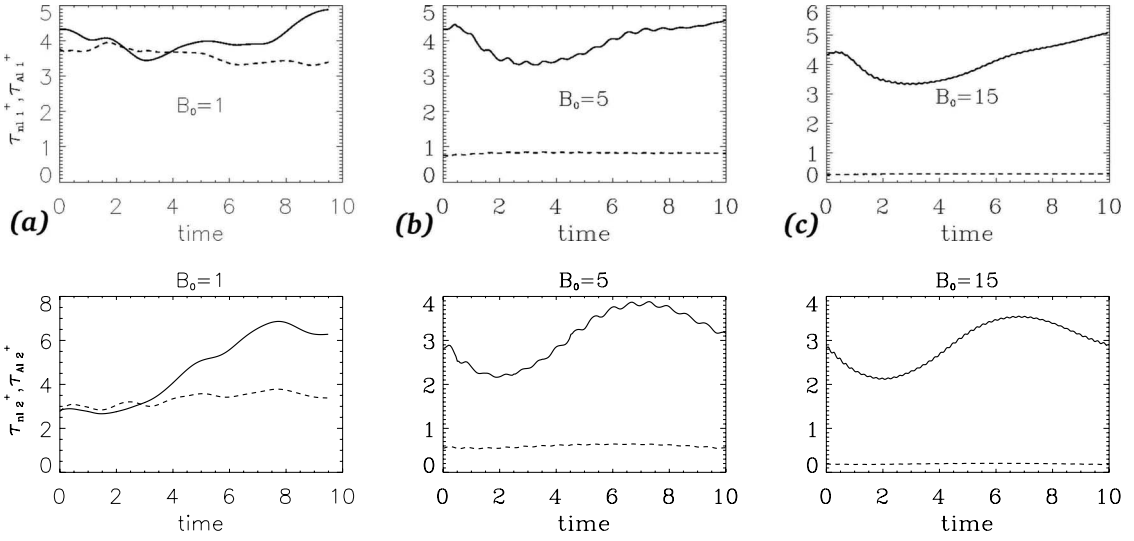

FIG. 12. Temporal evolution, up to $t=10$, of nonlinear (solid line) and Alfvén (dashed line) time scales for shear [(a)–(c)] and pseudo-Alfvén [(d)–(f)] waves for runs **IIa**–**IVa** (from left to right).

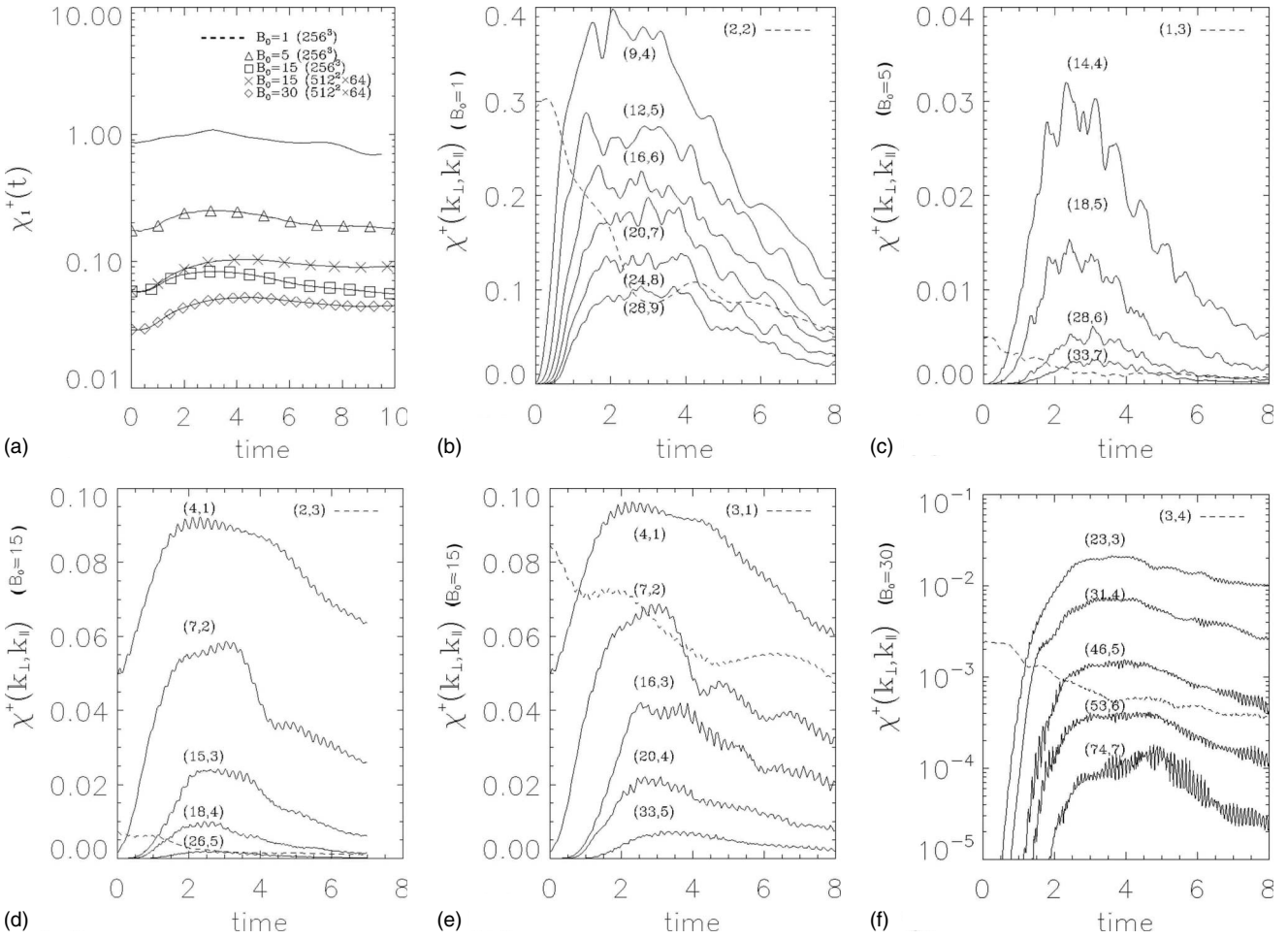

FIG. 13. Temporal evolution for shear-Alfvén waves of (a) the global ratio between the Alfvén and nonlinear time scales based on the anisotropic IK phenomenology (for runs **IIa**–**VIa**) and (b)–(f) same ratio at given $(k_\perp, k_\parallel)$ wave numbers (runs **IIa**–**VIa**): (b)–(d), runs **IIa**–**IVa**, with 256^3 resolution; and (e) and (f), runs **Va**–**VIa**, with $512^2 \times 64$ resolution. Note the use of a logarithmic coordinate in the (a) and (f) panels.

ure 15 shows that the temporal evolution of the different angles (for the different fields) is the same with a behavior depending mainly on the intensity of $\mathbf{B}_0$. For $B_0=0$ the energy transfer is similar in all directions and the temporal evolution of Shebalin angles remains almost constant, close to its initial value. For $B_0=5$ and $B_0=15$, the Shebalin angles quickly increase and stabilize around 78°. Thus, and as expected, the anisotropy develops with $\mathbf{B}_0$. However, the flow is not totally confined in planes perpendicular to $\mathbf{B}_0$ like for a purely bidimensional fluid for which the Shebalin angle is 90°. Note that a stronger anisotropy is produced for runs **Va** and **VIa** (for which the Reynolds number is higher) with angles up to 83°. This is explained by the wider range of $k_\perp$ available for such runs.

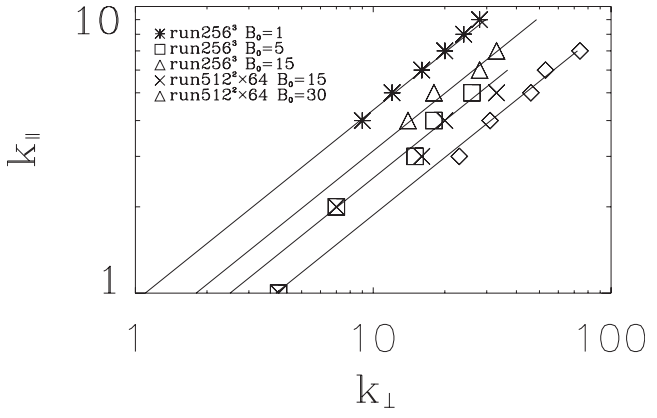

FIG. 14. Couples of points extracted from Fig. 13 well fitted by the anisotropic scaling law $k_\parallel \sim k_\perp^{2/3}$.

In Fig. 16, we report the generalized Shebalin angles for the vector fields $\mathbf{j}$, $\mathbf{w}$, and $\mathbf{w}^\pm$, where $\mathbf{w}^\pm = \nabla \times \mathbf{z}^\pm$. The same behavior as before is found with apparently a slightly stronger anisotropy (with angles closer to 90°) for the highest values of B_0. This is explained by the fields used, which are built on the rotational of the previous fields shown in Fig. 15 and thus to a higher dependence of relation (32) in perpendicular wave numbers (in $k_\perp^4$ instead of $k_\perp^2$).

IV. SPECTRAL ANALYSIS

A. Reduced spectra

Figures 17(a)–17(e) display the one-dimension (reduced) spectra

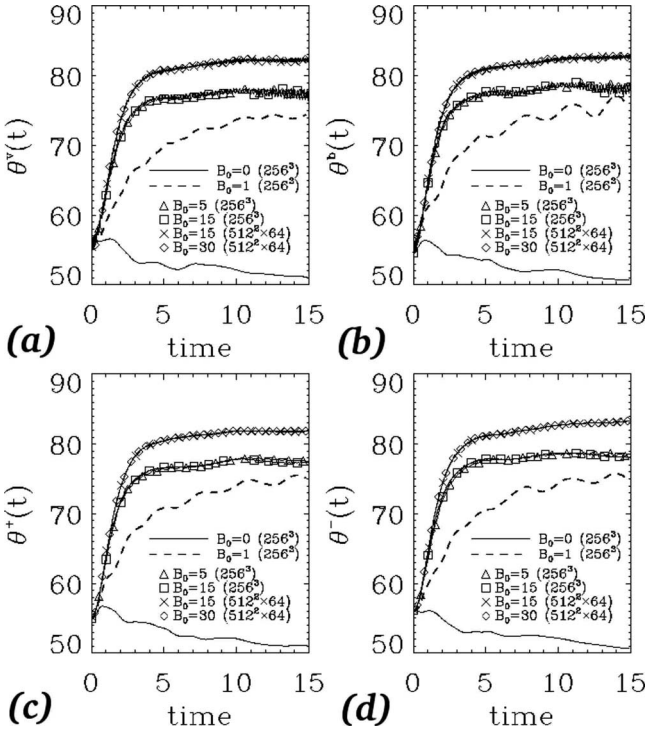

FIG. 15. Temporal evolution of generalized Shebalin angles for the (a) velocity, (b) magnetic, and (c) and (d) $z^{\pm}$ fields (runs **Ia**–**VIa**).

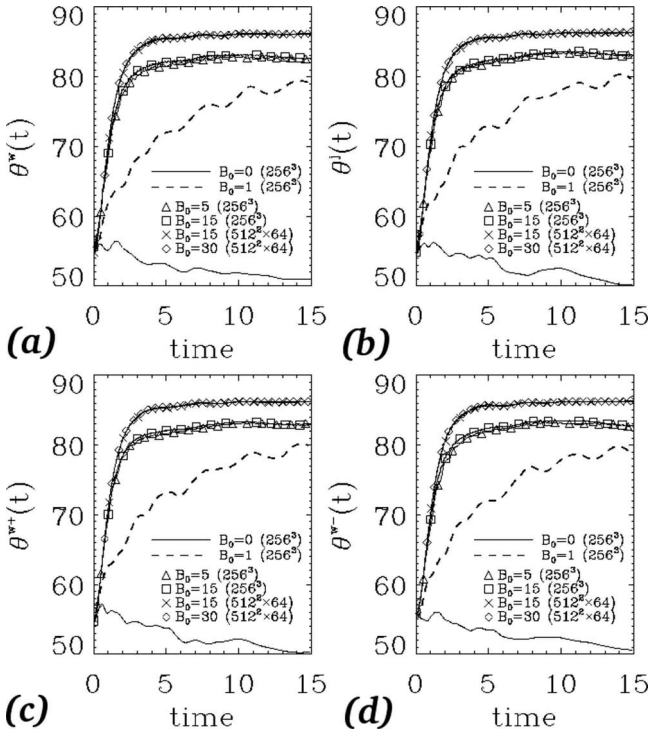

FIG. 16. Temporal evolution of generalized Shebalin angles for the (a) vorticity, (b) current density, and (c) and (d) $\omega^{\pm}$ vorticity fields (runs **Ia**–**VIa**).

$$E^+(k_x) = \int E^+(\mathbf{k}) dk_y dk_z, \tag{33}$$

$$E^+(k_y) = \int E^+(\mathbf{k}) dk_x dk_z, \tag{34}$$

$$E^+(k_z) = \int E^+(\mathbf{k}) dk_x dk_y, \tag{35}$$

for different B_0 intensity, with the same initial condition, and at times where the spectra are the most extended (i.e., $t \sim 2$ for runs **Ia** and **IIa**, $t \sim 3$ for **IIa** and **IVa**, $t \sim 4$ for **Va** and **VIa**). It basically illustrates the different spectral transfers in the perpendicular and parallel directions when the strength of the uniform magnetic field increases, whereas the x and y dependence is roughly the same. The equivalent spectra with polarity $-$ is not shown since it gives the same picture. Note that the scaling at large scales is not in contradiction with the initial condition discussed in Sec. II C, which concerns the modal spectrum.

B. Energy fluxes

In Fig. 17 (right) the associate reduced energy fluxes are given in k_x, k_y, and k_z. They are built from the Cartesian $\mathbf{z}^+$ fields. A constant flux is only found at the largest scales of the system. The presence of a negative flux is sometimes observed for a uniform field $B_0 \geqslant 5$. This property may be linked to the increase of the parallel length scale seen in Fig. 10. In this case, the flux is clearly not constant, which means that it is likely the result of a nonlocal interaction rather than an inverse cascade. Note that the same behavior is also found for the $-$ polarity.

The locality or nonlocality of the energy flux and transfer of runs **Ia**–**IVa** has been investigated recently [39] by means of different geometrical wave number shells. It is shown that the interactions between the two counterpropagating Elsässer waves may become nonlocal for strong magnetized flows. In particular, the energy flux in the $k_\perp$ direction is mainly due to modes that interact with the plane $k_\parallel = 0$ (with local interactions), while the weaker cascade in the parallel direction is due to modes that interact with $k_\parallel = 1$ (with possible nonlocal interactions) [39,40]. This property has been interpreted as a signature of a transition towards the weak turbulence regime during which the number of effective modes in the energy cascade is reduced.

C. Anisotropic spectra

Figure 18 shows anisotropic spectra for shear-Alfvén waves (polarity $+$) at times for which turbulence is fully developed ($t \sim 4$). First, we see spectra $E_1^{\pm}(k_\perp)$ (top), which are defined as

$$E_1^{\pm}(k_\perp) = \int E_1^{\pm}(k_\perp, k_\parallel) dk_\parallel. \tag{36}$$

Then two other sets of spectra are given: $E_1^{\pm}(k_\perp, k_\parallel = 0)$ and $E_1^{\pm}(k_\perp, k_\parallel = 1)$ (the middle and bottom panels, respectively). The most interesting case seems to be the middle panel, i.e., the spectra of the two-dimensional (2D) state, from which we

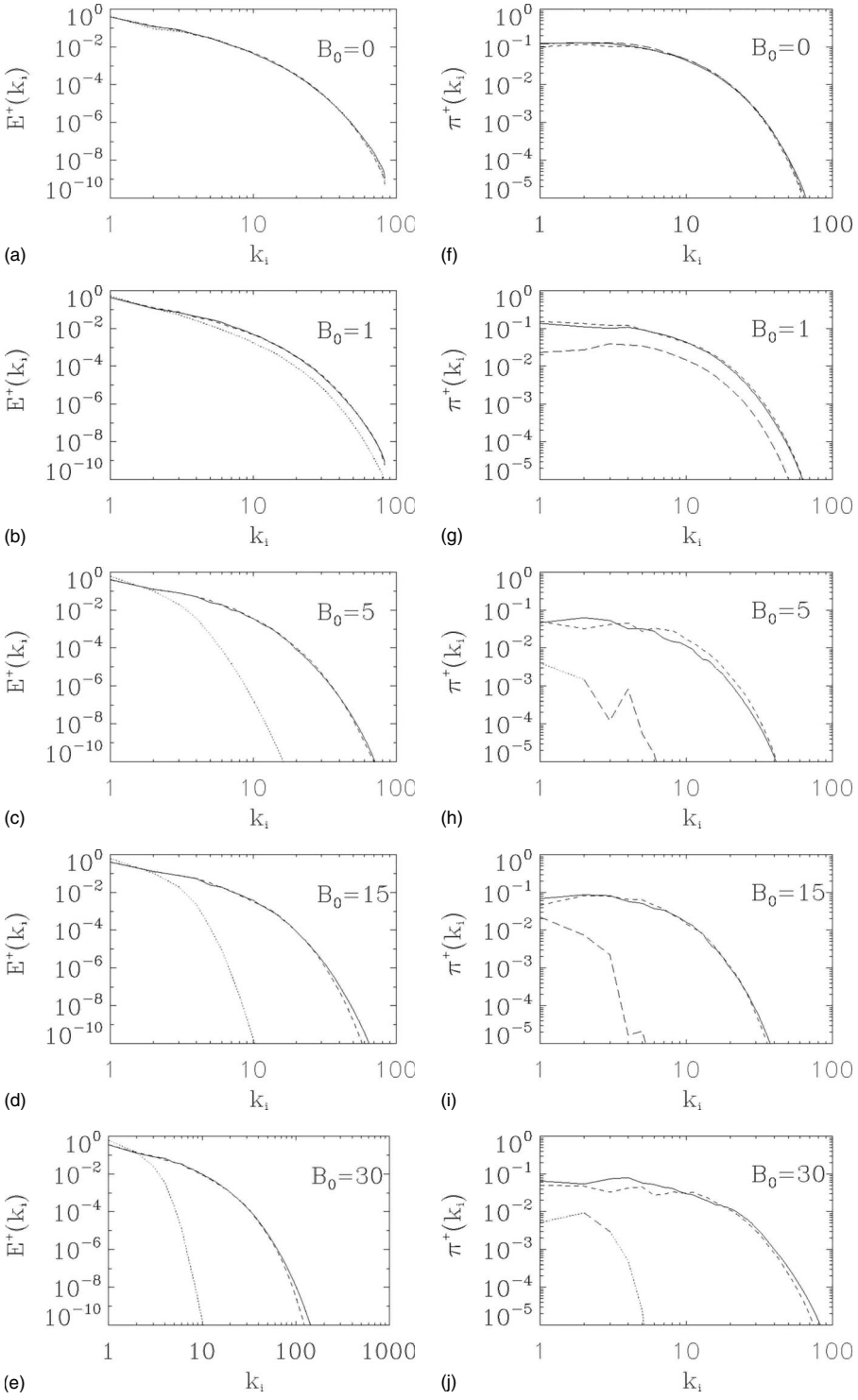

FIG. 17. [(a)–(e)] Reduced spectra E^+ built from the Cartesian fields $\mathbf{z}^+$. [(f)–(j)] The associated reduced energy fluxes Π^+ for the variables k_x (solid line), k_y (dashed line), and k_z (dotted line for E^+ and long-dashed line for Π^+). In the latter case when a negative flux is found, the absolute value is taken (dotted line). (Runs **Ia**–**IVa** and run **VIa**, from top to bottom.)

see a clear inertial range where a power law may be extracted. An attempt is made to find this power law by computing the compensated spectra $E^+E^-k^m$. Different values are proposed in the insets. We see that the 2D state is characterized by approximately $m=14/3$, which means on average a spectrum steeper than the Kolmogorov one. This scaling is clearly different from the value found for $E_1^{\pm}(k_\perp)$ where the Kolmogorov value $m=10/3$ is better fitted. The last case $E_1^{\pm}(k_\perp, k_\parallel=1)$ is the most difficult one to analyze and no clear scaling appears. Note that the hyperviscous runs do not exhibit significant differences with, for example, a wider inertial range. In fact, the latter effect is easier seen for spectra plotted at fixed, but large, $k_\parallel$ ($k_\parallel>1$). Finally, note the difference between these spectra and those found in Figs.

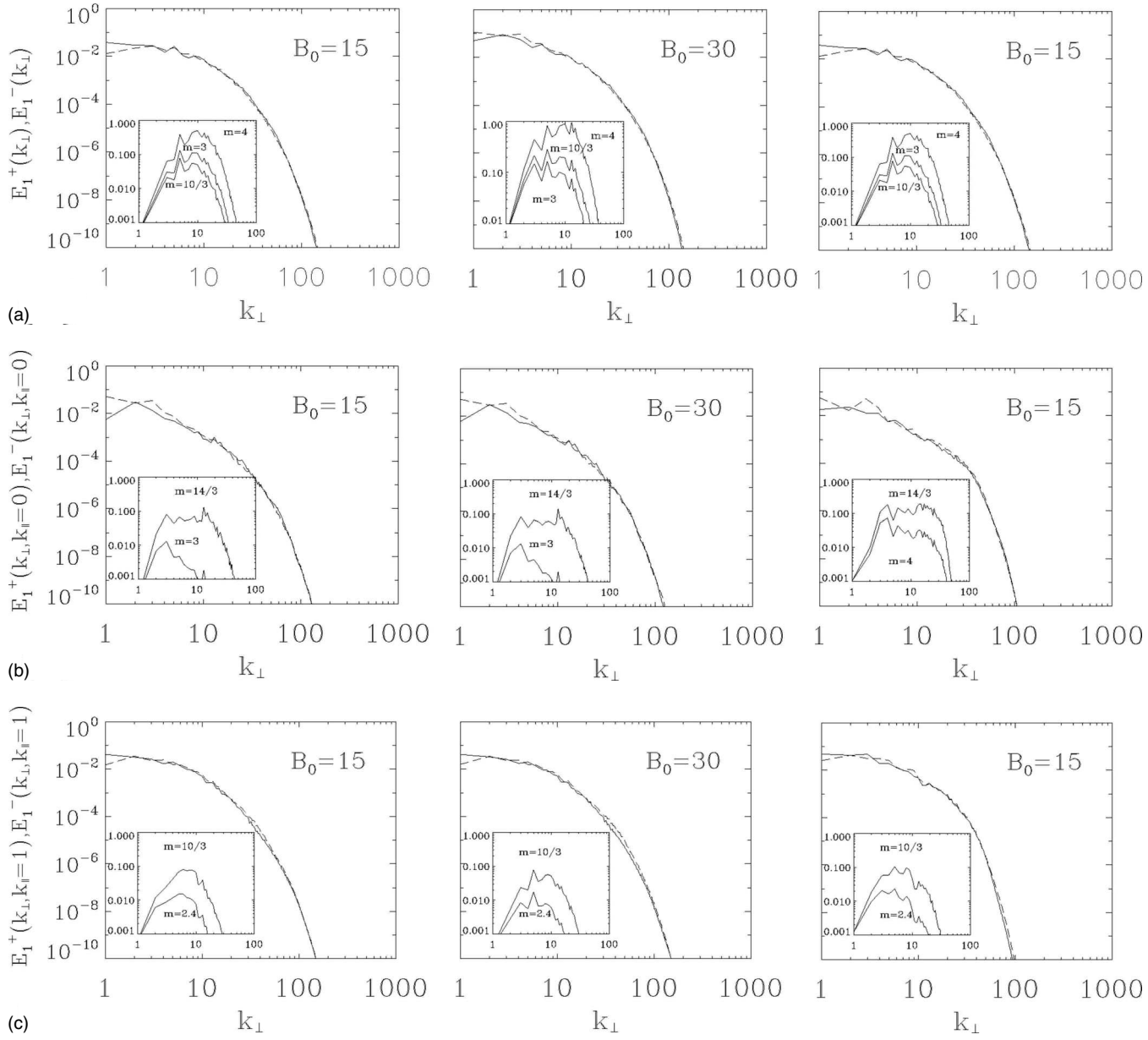

FIG. 18. Energy spectra of shear-Alfvén waves E_1^+ (solid line) and E_1^- (dashed line) vs the perpendicular wave numbers $k_\perp$ after integration over all parallel wave numbers (a), for $k_\parallel=0$ (b) and for $k_\parallel=1$ (c). Each of these three columns presents, from left to right, respectively, runs **Va** and **VIa** ($512^2\times64$ resolution, $\nu=10^{-3}$ with $B_0=15$ and 30), and the hyperviscous run **VIIa** ($512^2\times64$ resolution, $\nu=10^{-6}$ with $B_0=15$). Insets: compensated product of energy spectra, $E^+E^-k^m$ for a given m as indicated in the insets.

17(a)–17(e) with an inertial range easier to determine in Fig. 18, which may be attributed to the choice of the representation (anisotropic spectra instead of reduced spectra).

D. Anisotropic scaling laws

In order to extract a scaling law between parallel and perpendicular wave numbers, we plot the modes $(k_\perp,k_\parallel)$ corresponding to the equality $E_1^+(k_\perp)=E_1^+(k_\parallel)$ with

$$E_1^+(k_\parallel)=\int E_1^+(k_\perp,k_\parallel)dk_\perp. \tag{37}$$

The result is given in Fig. 19 for runs **IIa** ($t\sim2$), **IIIa**–**IVa** ($t\sim3$) and **VIa** ($t\sim4$). We clearly see different slopes for different magnitudes of B_0, with an isotropic law $k_\parallel\sim k_\perp$ for $B_0=1$ and an anisotropic law around $k_\parallel\sim k_\perp^{2/3}$ for $B_0\geqslant15$ (see the insets). For all cases, we see that the scaling law extends to the dissipative range. The same behavior is found for the pseudo-Alfvén waves (not shown here). Note that with this method the scaling law extracted suffers from an average effect since each spectrum is obtained after summation over the parallel or the perpendicular direction. Nevertheless, the anisotropic prediction proposed by [10] is often recovered, but as it was explained above for a subcritical balance between the Alfvén and nonlinear times, which may be understood in a wider context [27] as discussed in the Introduction.

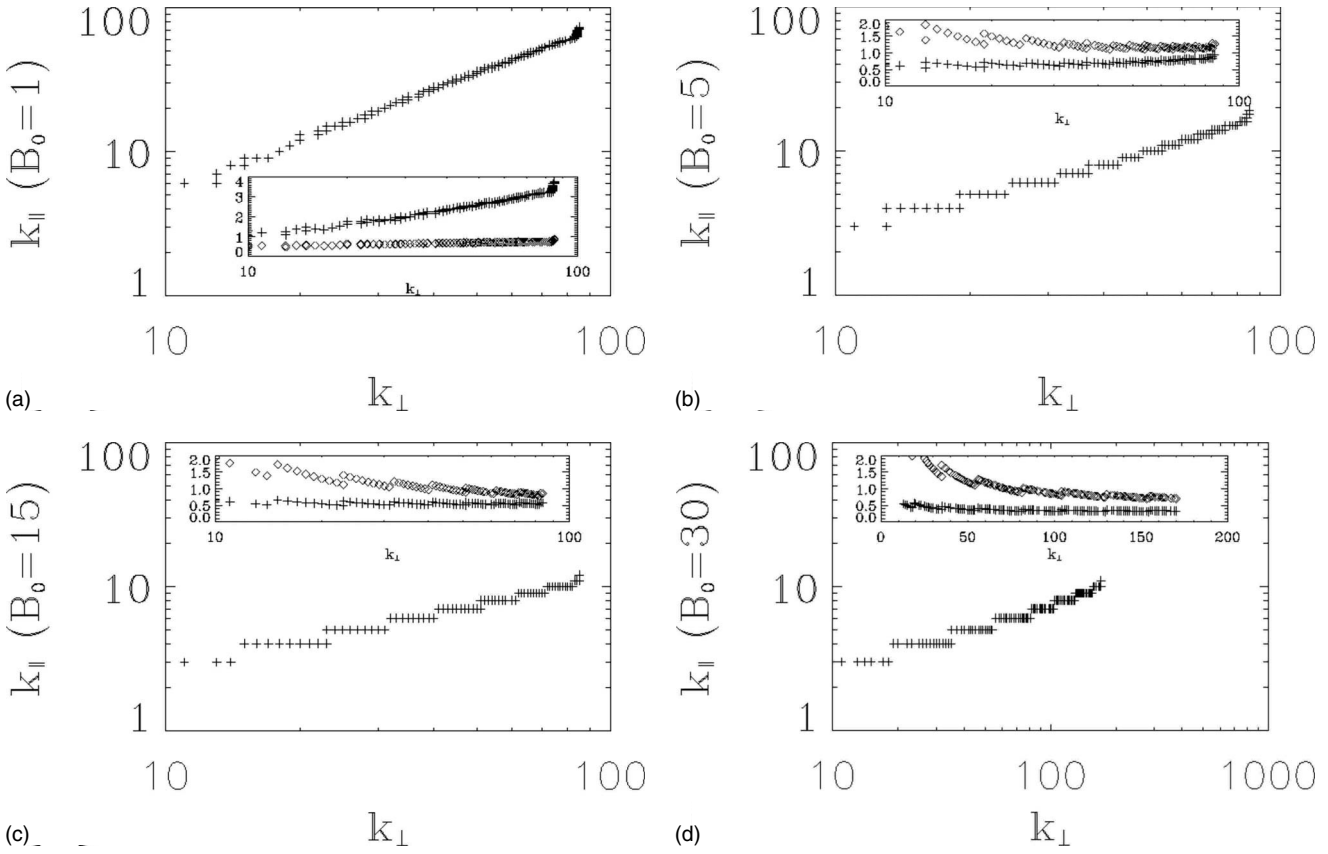

FIG. 19. Anisotropic scaling laws between wave numbers $k_\perp$ and $k_\parallel$ (see the text): (a)–(c) for runs **IIa**–**IVa** (256^3) and (d) run **VIa** ($512^2\times64$). The inset displays two compensated scalings: $k_\parallel(k_\perp)k_\perp^{-1}$ (diamonds) and $k_\parallel(k_\perp)k_\perp^{-2/3}$ (crosses).

V. VISUALIZATIONS

A. Spectral space

At a time at which energy spectra are fully developed, Fig. 20 displays perpendicular, at $k_\parallel=0$, and parallel, at $k_y=0$, cuts in Fourier space for $E^+(\mathbf{k})$ in flows at $\nu=\eta=4\times10^{-3}$ without ($B_0=0$, $t=2$; run **Ia**) or with ($B_0=15$, $t=3$; run **IVa**) an applied magnetic field. Initially, for both flows, the isotropic energy injection corresponds to spherical shells with maximum radius $k=8$. The spectra then evolves depending on the level of the flow magnetization. Indeed, at $B_0=0$, the maximum spectral radius increases in all directions, meaning an isotropic energy transfer towards small scales, while at $B_0=15$, the three-dimensional energy spectrum collapses into ellipsoidal shapes with ratio 1/6, corresponding to an anisotropic transfer, strongly inhibited in the $\mathbf{B_0}$ parallel direction. In this case, in $\mathbf{B_0}$ perpendicular planes (shown here at $k_\parallel=0$), one can observe a loss of excitation at higher modes together with a loss of axisymmetry, with two preferred directions, compared to nonmagnetized flows.

Figure 21 shows the case of strongly magnetized flows, $B_0=30$, at lower viscosity $\nu=10^{-3}$, and resolved with $512^2\times64$ grid points ($t=4$; run **VIa**). The aspect ratio of the spectral ellipsoidal shape decreases up to 1/10 and in transverse planes, a star shape with several "jets" appears. As time evolves (not shown), the number of these jets increases leading to an enhanced isotropy in tranverse planes (at $k_\parallel\geqslant0$). In all flows, similar observations stand for $E^-(\mathbf{k})$ spectra.

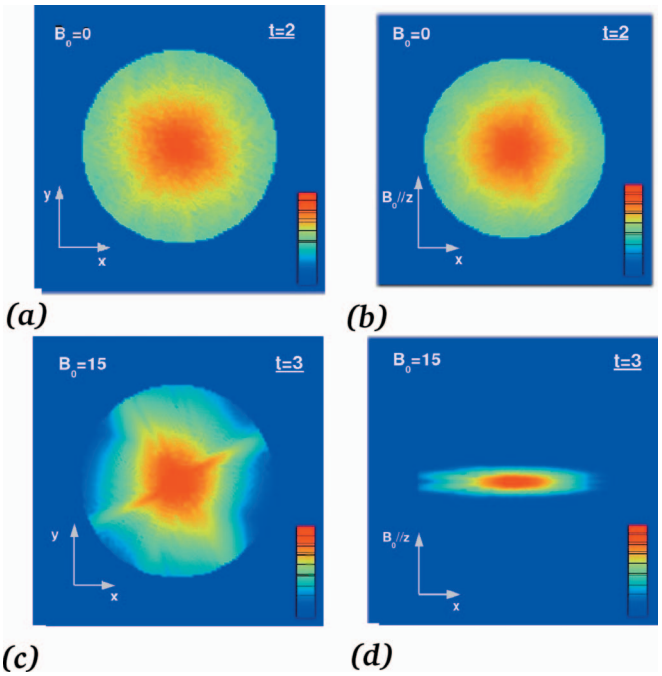

FIG. 20. (Color) $E^+(\mathbf{k})$ cuts in Fourier space at $k_\parallel=0$ [(a) and (c)] and $k_y=0$ [(b) and (d)] for flows at $B_0=0$ (run **Ia** with 256^3) at $t=2$, and $B_0=15$ (run **IVa** with with 256^3) at $t=3$. Color bars are normalized to 1 for the maximum intensity (red) and to 0 for the minimum (blue) one.

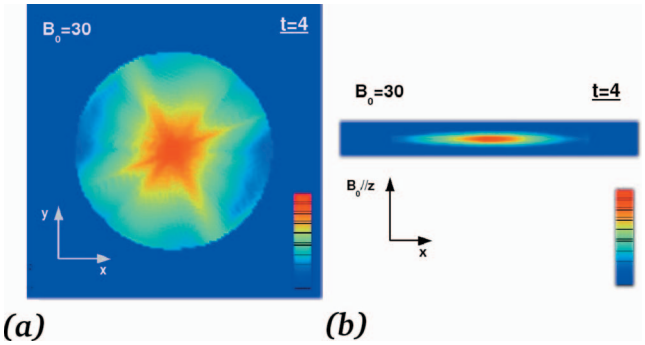

FIG. 21. (Color) $E^+(\mathbf{k})$ cuts in Fourier space at (a) $k_\parallel=0$ and (b) $k_y=0$ for flows at $B_0=30$ (run **VIa** using $512^2\times64$ grid points) at $t=4$. Color bars are normalized to 1 for the maximum intensity (red) and to 0 for the minimum (blue) one.

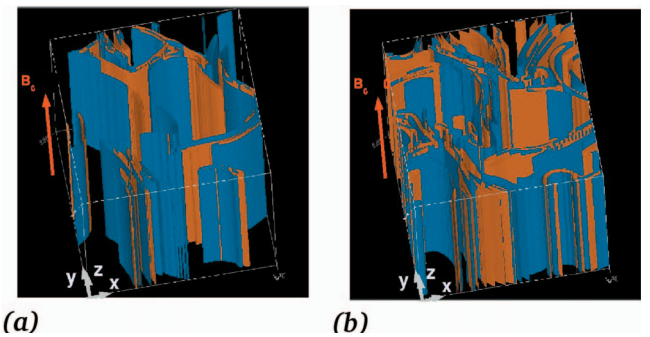

FIG. 22. (Color) Isosurfaces of vorticity (blue) and current (orange) intensities for the 2D state $k_\parallel=0$ (see the text) for a flow with $B_0=30$ (run **VIa**, $512^2\times64$), drawn at 20% of their respective maxima: (a) at $t=4$, $|\mathbf{w}|_{max}=8.8$ and $|\mathbf{j}|_{max}=11.3$, and (b) at $t=6$, $|\mathbf{w}|_{max}=6.6$ and $|\mathbf{j}|_{max}=8.1$.

B. Physical space

In order to understand the observed spectral structures in transverse planes for magnetized flows, we first visualize their spatial counterparts, once some Fourier amplitudes at wave vectors $(k_x,k_y,k_z=k_\parallel)$ are filtered for a given field. Hence structures only corresponding to the 2D state are obtained with $(k_x,k_y,k_\parallel>0)$ modes filtered, and structures for 3D modes $(k_\parallel>0)$ are obtained with $(k_x,k_y,k_\parallel=0)$ modes filtered. Figure 22, for a flow with $B_0=30$ (run **VIa**), displays vorticity and current isosurfaces for the 2D state at the same time as Fig. 21, $t=4$, and at a later time $t=6$. The transverse spectral star shape is related to the spatial distribution of the vorticity and current sheets, perpendicularly to two peculiar directions at $t=4$, and more irregularly distributed at $t=6$ for which a higher number of jets is observed in spectral transverse planes (not shown).

Similarly, for a flow with $B_0=15$ (run **Va**), vorticity and current isosurfaces for states with $k_\parallel=0$ and $k_\parallel>0$ are shown in Fig. 23 at $t=7$, when the total energy loss is about 20%. The 2D state structures are again related to the star shape observed in transverse spectral planes (not shown), while the vorticity and current sheets with $k_\parallel>0$ present filamentary structures. This filamentation is an important result. Indeed, in the literature, until now the current and vorticity structures were mainly described as smooth sheets in the numerical (strongly) magnetized flows.

When looking at the dynamics in physical space (without filtering), shown in Fig. 24, the vorticity and current intensities are superimposed sheetlike structures aligned along the ambient magnetic field. At $t=7$, a filament formation is observed within the sheets. This can be related to the filamentary structures with $k_\parallel>0$ (see Fig. 23) that do not exist in the 2D state, meaning that this sheet filamentation is mainly due to the wave components. At later times, $t=10$, with a total energy loss of about 55%, the vorticity and current sheets are disruped by dissipation effects.

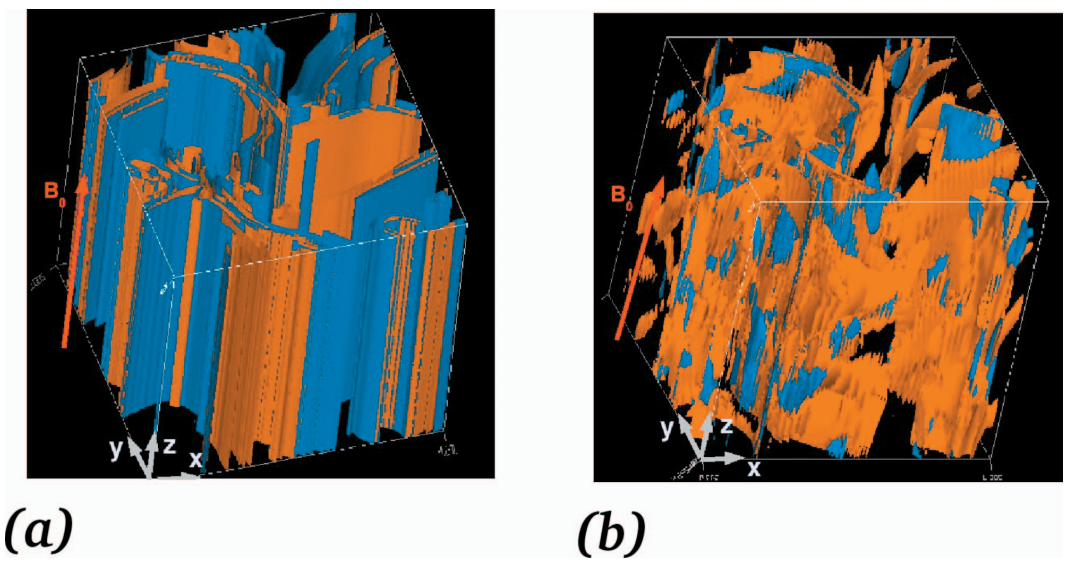

FIG. 23. (Color) Filtered vorticity (blue) and current (orange) intensities with (a) $k_\parallel=0$ (2D state) and (b) $k_\parallel>0$, for $B_0=15$ (run **Va**, $512^2\times64$) at $t=7$: isosurfaces are drawn at 27% and 20% of their respective maxima ($k_\parallel=0$; $|\mathbf{w}|_{\max}=5.7$ and $|\mathbf{j}|_{\max}=9$, and $k_\parallel>0$; $|\mathbf{w}|_{\max}=18.5$ and $|\mathbf{j}|_{\max}=19.2$).

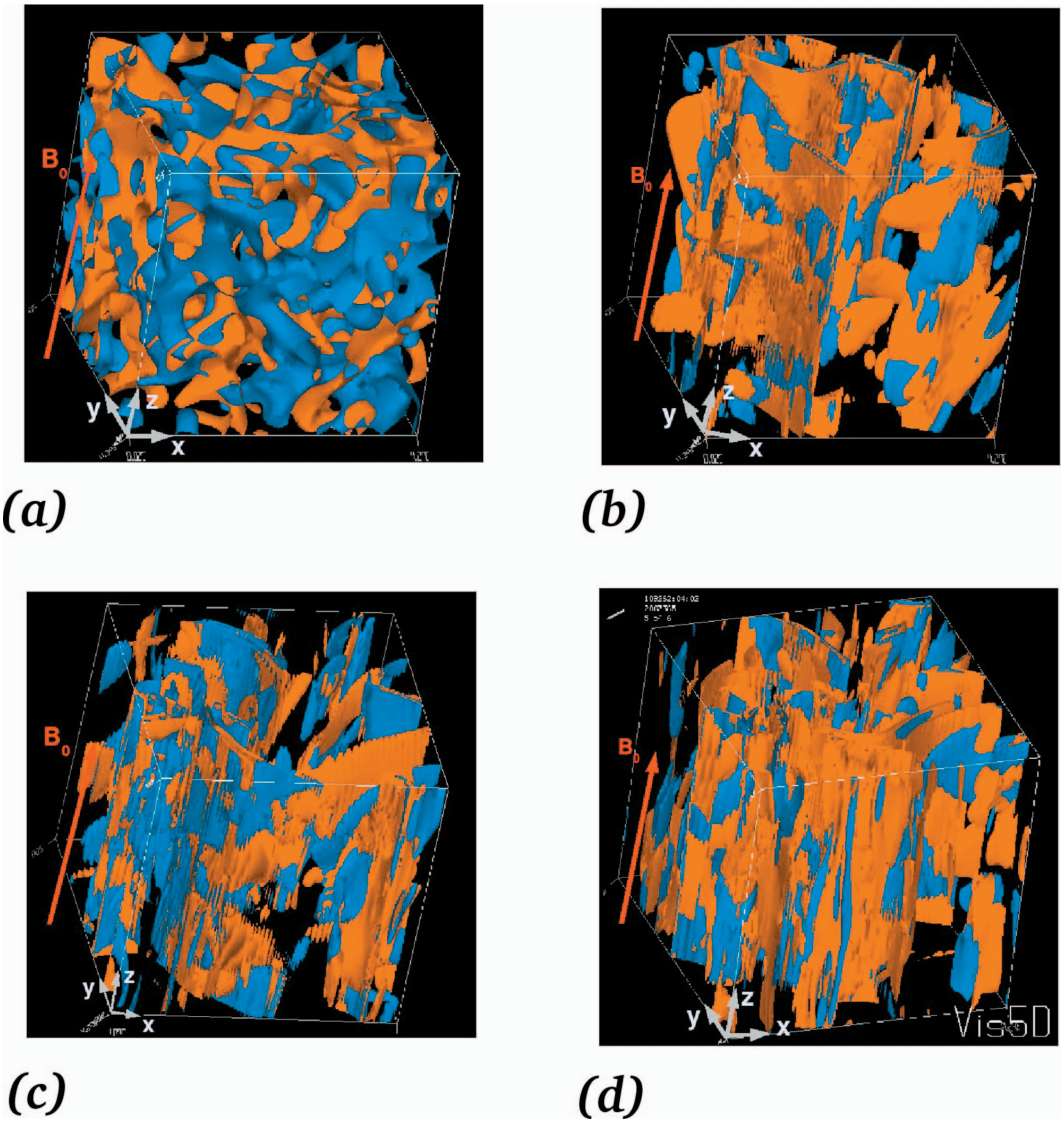

FIG. 24. (Color) Temporal evolution of vorticity (blue) and current (orange) intensities for the same run as in Fig. 23. Isosurfaces are drawn at 27% and 20% of $|\mathbf{w}|_{\max}$ and $|\mathbf{j}|_{\max}$ instantaneous maxima. (a) At $t=0$; $|\mathbf{w}|_{\max}=2.7$ and $|\mathbf{j}|_{\max}=3$. (b) At $t=4$; $|\mathbf{w}|_{\max}=24.3$ and $|\mathbf{j}|_{\max}=27.6$. (c) At $t=7$, $|\mathbf{w}|_{\max}=17.9$ and $|\mathbf{j}|_{\max}=25.6$. (d) At $t=10$, $|\mathbf{w}|_{\max}=9.2$ and $|\mathbf{j}|_{\max}=15.4$.

Figure 25 shows the distribution of the cross-correlation values at $z=\pi$ [(a) and (b)] and in the entire numerical box [(c) and (d)]. A comparison with the current and vorticity distribution shows that the high (absolute) value of the cross correlation coincides with the position of dissipative structures, which means that the velocity and magnetic field fluctuations tend to be aligned at small scales. This result corroborates recent works on the dynamic alignment in MHD [41] where a statistical model is proposed.

VI. RUNS Ib AND IIb

In a last set of simulations we change the initial condition, as explained in Sec. II C 3, to evaluate, in particular, their influence on the dynamics. It is thought that this new initial condition is more appropriate to turbulent flows with a modal spectrum at large scales (larger than the integral length scale) in $k_\perp^3$, which is in agreement with the phenomenology for freely decaying turbulence [23]. These runs correspond to a strong magnetized flow ($B_0=15$) and high resolution ($512^2 \times 64$). We will not focus on the temporal decay that has been analyzed recently [23] and we will only look at the spectral behavior.

In Fig. 26 we show the 1D spectra $E^+_{1,2}(k_\perp)$ for shear- and pseudo-Alfvén waves integrated over all parallel wave numbers. The time chosen is the one for which we have a fully developed turbulence. Despite the high resolution no clear inertial range appears. The Kolmogorov scaling is given as a reference that is roughly followed.

Figure 27 gives at the same time the energy spectra $E^+_{1,2}$ and $E^-_{1,2}$ of shear- and pseudo-Alfvén waves for the 2D state ($k_\parallel=0$). The most remarkable result is the presence of a relatively extended inertial range characterized by a compensated energy spectrum on average around the IK prediction, i.e., in $k_\perp^{-3/2}$ (note, however, the presence of a bottleneck

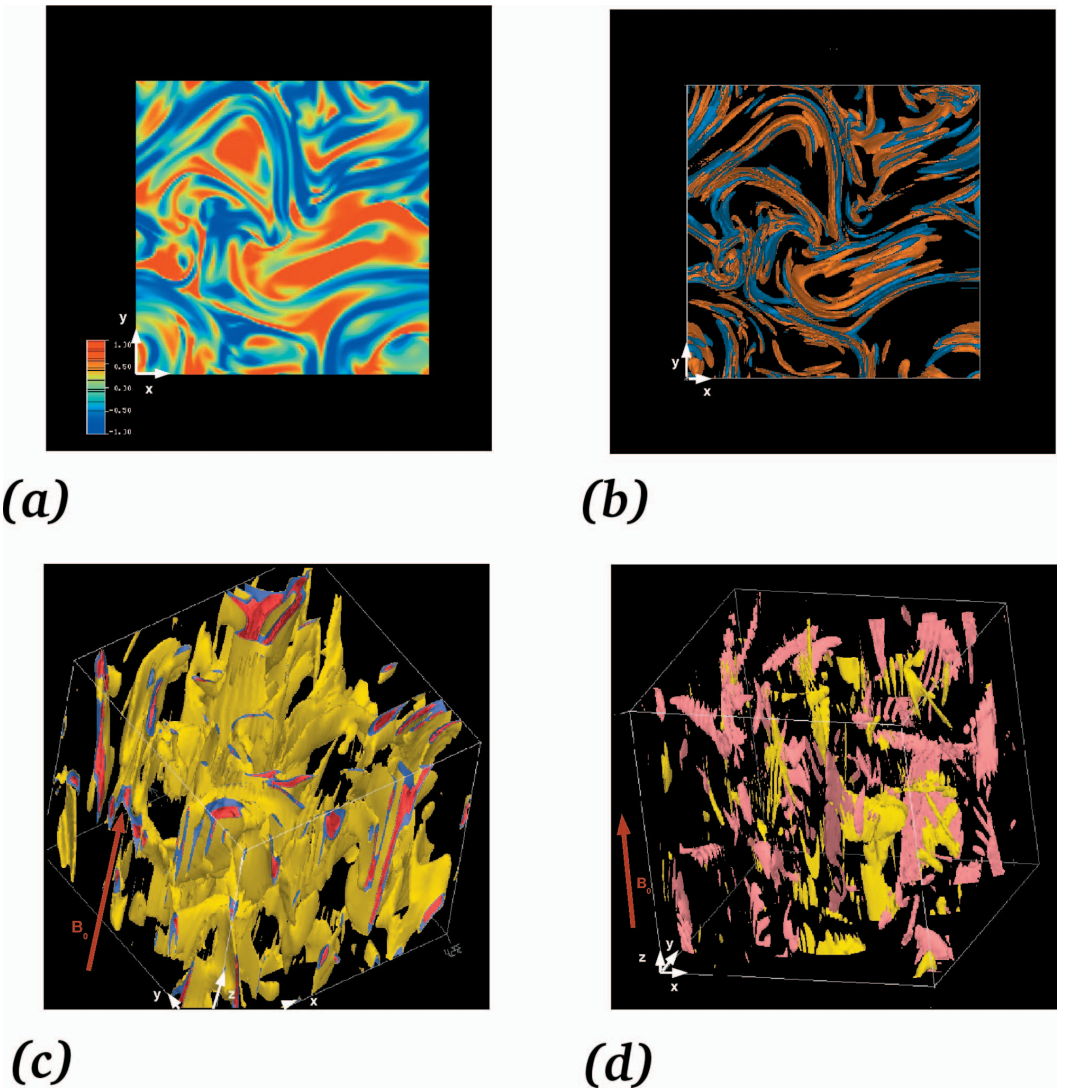

FIG. 25. (Color) (a) Isosurfaces (at $z=\pi$) of the cross-correlation coefficient. (b) The corresponding isosurfaces of the current (red) and vorticity (blue) drawn at 21% of their respective maxima. (c) Isosurfaces of the cross-correlation coefficient at −0.70 (yellow), −0.75 (blue), and −0.90 (red). (d) Isosurfaces of the cross-correlation coefficient at 0.96 (yellow) and −0.96 (pink). (Run **Va** at time $t=10$.)

effect for the viscous run [(a) and (c)]. We conclude that the integration over the parallel wave numbers tends to hide the true scaling by an average effect.

Figure 28 gives at the same time the energy spectra $E^{+}_{1,2}$ and $E^{-}_{1,2}$ of shear- and pseudo-Alfvén waves at a fixed parallel wave number ($k_{\|}=1$). Once again a relatively extended inertial range is found. It is characterized by a compensated energy spectrum steeper than the previous one with an index around $k_{\perp}^{-2}$ and $k_{\perp}^{-7/3}$ for, respectively, the hyperviscous and viscous case. Other spectra at higher fixed parallel wave numbers are not shown because they are characterized by a smaller inertial range from which it is difficult to find a power-law scaling.

VII. SUMMARY AND CONCLUSION

In this paper, we present a set of three-dimensional (3D) direct numerical simulations of incompressible decaying MHD turbulence in which the influence of an external uniform magnetic field $\mathbf{B_0}$ is investigated. A parametric study in terms of B_0 intensity is made to show the development of anisotropy. In general, the temporal evolutions show oscillations that are associated with the presence of Alfvén waves. The dynamics is slower for strongly magnetized flows with, in particular, a cross correlation between the velocity and the magnetic field fluctuations frozen on average around its initial (small) value but with, locally, a wide range of possible values. For all temporal results, one can see that the flows with the highest values of B_0 ($\geqslant 5$) behave quite similarly while for $B_0=1$, the flow presents a transient regime between the case without background magnetic field and the other cases. We also discuss the presence of a subcritical balance between the Alfvén and nonlinear times with both a global and a spectral definition. This regime is still associated with the anisotropic scaling laws (1) between the perpendicular and the parallel wave numbers. The nonlinear dynamics of

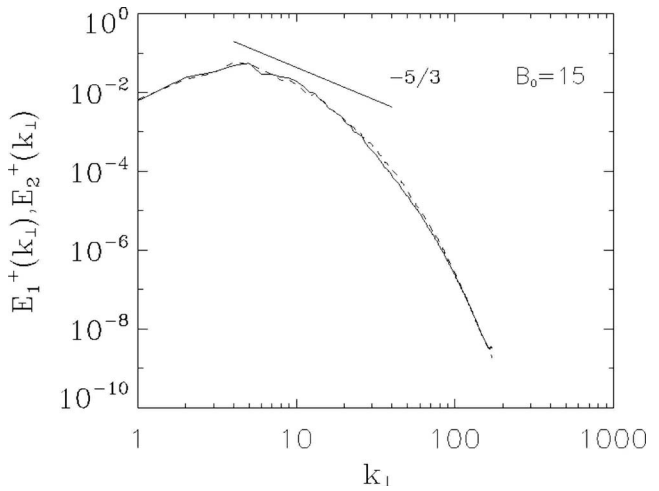

FIG. 26. Energy spectra $E^+_{1,2}(k_\perp)$ for shear-(solid) and pseudo-Alfvén (dashed line) waves integrated over all parallel wave numbers in the viscous case (run **Ib**, $512^2\times 64$). The straight line follows a $k_\perp^{-5/3}$ law.

strongly magnetized flows is characterized by a different $k_\perp$ spectrum if it is plotted at a fixed $k_\parallel$ (2D spectrum) or if it is integrated (averaged) over all $k_\parallel$ (1D spectrum). In the former case a much wider inertial range is found with a steep power law, closer to the wave turbulence prediction than the Kolmogorov one like in the latter case. Note that the inertial range of these spectra is better seen for the shear- and pseudo-Alfvén waves rather than for the Cartesian fields.

One of the most important results of this paper is the difference found between the $k_\perp$ spectra plotted after integration over $k_\parallel$ and those at a given $k_\parallel$. This point is generally not discussed in numerical works, whereas it appears to be a fundamental aspect of this problem. Direct numerical simulations of the Alfvén wave turbulence regime seems to be still out of the current numerical capacity [33] and only the detection of the transition towards such a regime seems possible. In such a study it is crucial to avoid any noisy effect linked, for example, to the initial condition (or forcing) that could favor one particular type of spectrum. But the other

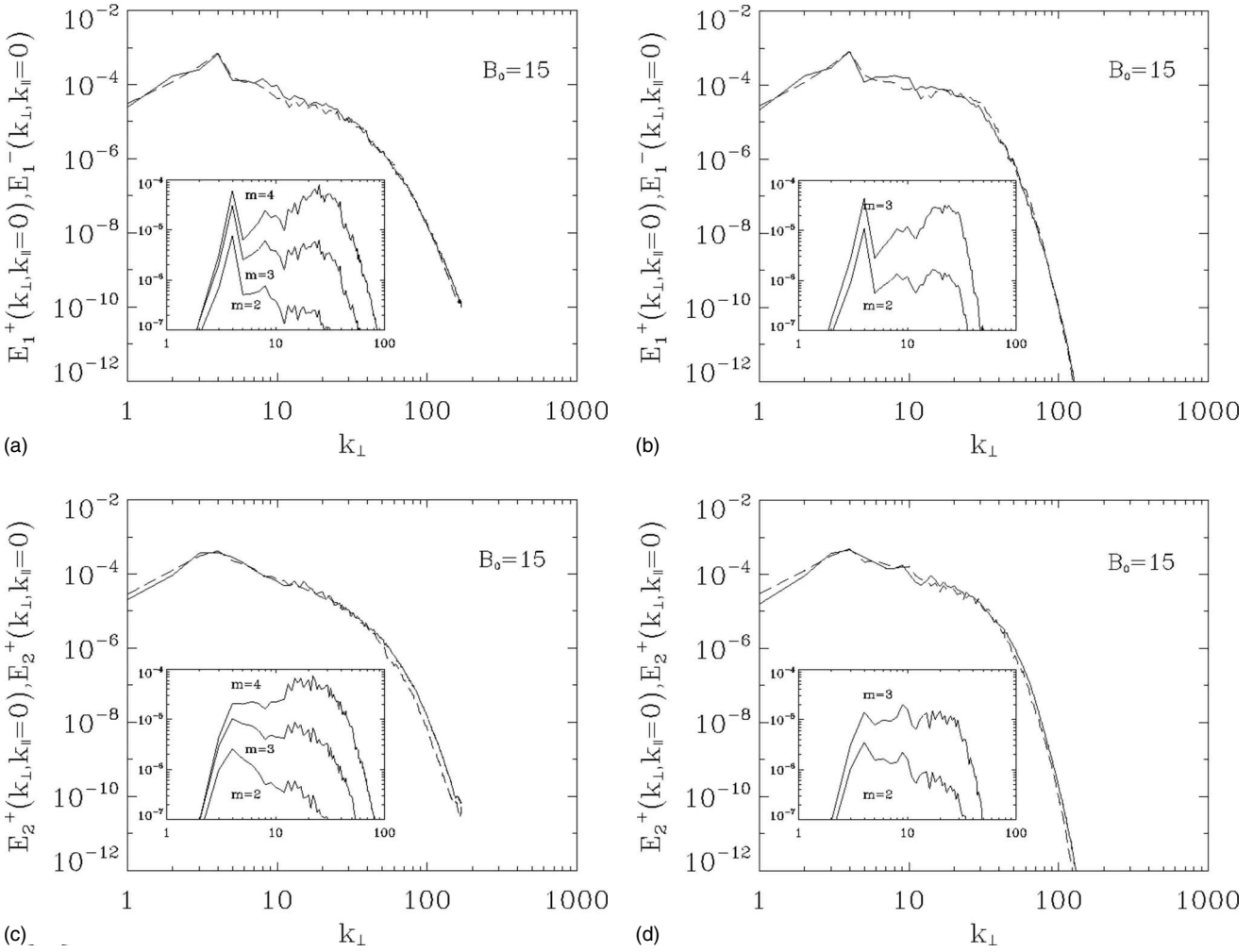

FIG. 27. Energy spectra $E^+_{1,2}$ (solid) and $E^-_{1,2}$ (dashed) of shear [(a) and (b)] and pseudo [(c) and (d)] Alfvén waves for the 2D state ($k_\parallel$=0). The viscous (run **Ib**, $512^2\times 64$) [(a) and (c)] and the hyperviscous case (run **IIb**, $512^2\times 64$) [(b) and (d)] are shown. Inset: Compensated energy spectra $E^+_{1,2}(k_\perp,0)E^-_{1,2}(k_\perp,0)k^m$, with a given value of m as indicated in the insets.

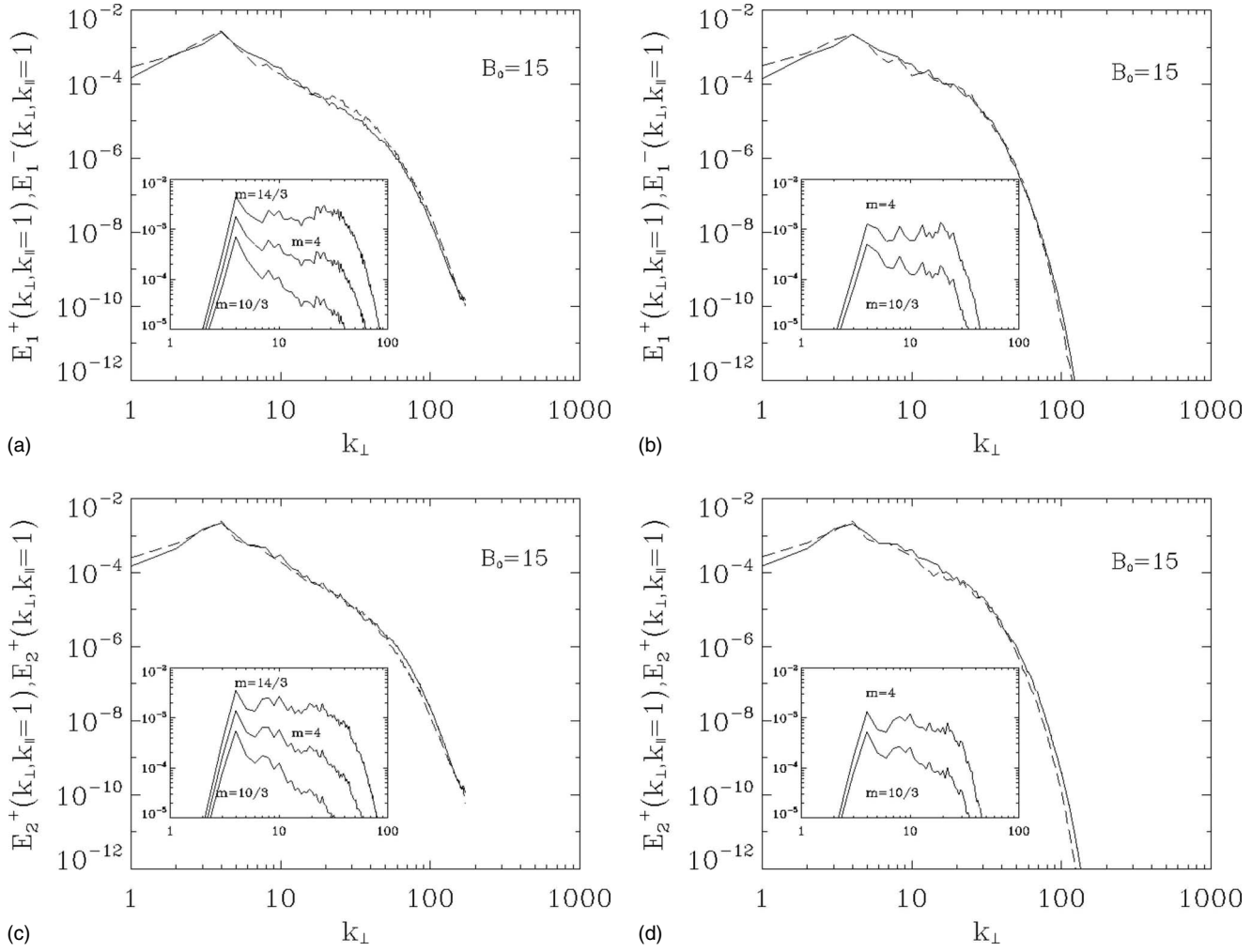

FIG. 28. Energy spectra $E^{+}_{1,2}$ (solid) and $E^{-}_{1,2}$ (dashed) of [(a) and (b)] shear-Alfvén waves and [(c) and (d)] pseudo-Alfvén waves for $k_{\parallel}=1$. The viscous [(a) and (c); run **Ib**, $512^2\times 64$] and the hyperviscous case [(b) and (d); run **IIb**, $512^2\times 64$] are shown. Inset: compensated energy spectra $E^{+}_{1,2}(k_{\perp},1)E^{-}_{1,2}(k_{\perp},1)k^m$, with a given value of m as indicated in the insets.

effect that could hide the true dynamics of strongly magnetized flows is the averaging effect as we have clearly seen in the second set of simulations: the presence of an inertial range was not obvious from a first global analysis (Fig. 26), whereas it was clear from the 2D spectra (Fig. 27). This averaging effect may be due to the moderate spatial resolution used but also to the regime that is in a transition phase towards the wave turbulence regime. If we extrapolate such a result to natural plasmas like the one found in the interplanetary medium (inner solar wind) then we may interpret the current spectra as averaging spectra (since we are not able to report spectra at a given parallel wave number with only one spacecraft). Then it is not surprising that we observe both an anisotropic flow with approximately a Kolmogorov scaling.

In a recent numerical analysis [34] dedicated to the development of anisotropy and wave turbulence in forced incompressible reduced MHD flows, a change of spectral slope was reported for the $k_{\perp}$-energy spectrum when the forcing is applied on a larger range of parallel wave numbers with no driving of the $k_{\parallel}=0$ modes. In the light of the present paper this finding may be interpreted as a way to decrease the averaging effect, which is mainly due to the dissipative scales. Indeed, when a larger parallel wave number is excited the spectrum integrated over all $k_{\parallel}$ is more sensitive to the nondissipative parallel wave numbers and tends therefore to reveal the true scaling. Another way to avoid this noisy effect would have been to plot the spectra at a given but low parallel wave number in order to avoid the dissipative range.

The question of the power-law index predicted by the wave turbulence theory has not been addressed so far. A $k_{\perp}^{-2}$ spectrum is expected for strongly magnetized flows in the regime of wave turbulence (even without assuming a restriction on $k_{\perp}$ and $k_{\parallel}$ [42]). In our simulations a scaling close to this value is found when hyperviscosity is used (Fig. 28) in the second set of simulations at $k_{\parallel}=1$, whereas the 2D state (spectrum at $k_{\parallel}=0$) scales on average around $k_{\perp}^{-3/2}$. This latter result is the same as the one found generally in 2D isotropic MHD turbulence [43,44]. The steep power law reported in $k_{\perp}^{-\alpha}$ with $\alpha\in[2,7/3]$ may be attributed to the very first sign of the wave turbulence regime that should be confirmed nevertheless at higher resolution. The $\alpha=7/3$ case is *a priori* unexpected although it was seen as a transient regime before the finite energy flux solution settles down [14]. However, no change of slope is observed in our simulation because, in

particular, for larger times the reduction of the inertial range does not allow one to conclude about the inertial scaling law. The case $\alpha=7/3$ is also a solution predicted by a heuristic model based on a subcritical balance between the Alfvén and the nonlinear times [27]. In this case, the total energy spectrum satisfies the relations $E(k_\perp,k_\parallel)\sim k_\perp^{-\alpha}k_\parallel^{-\beta}$, with $3\alpha+2\beta=7$. Thus the $\alpha=7/3$ solution implies no $k_\parallel$-scale dependence, which could be linked to the weakness of parallel transfers.

Our analysis in the physical space has revealed important information about structures. A filament formation is observed within the current and vorticity sheets. This important property may be explained by the specific condition of our simulation (large B_0 and large Reynolds number) and has to be confirmed at higher Reynolds numbers. The classical picture of current sheets in MHD turbulence may be wrong in the strongly anisotropic case and filaments may be the right picture. This result may be compared with astrophysical plasmas like in the solar corona where extremely thin (dissipative) coronal loops (filaments or "strands") are observed. Although their presence is well accepted, the origin of these filaments is still not well explained. Turbulence and Alfvén wave could be the main ingredients [45].

Other questions about scaling laws for structure functions and intermittency for strongly magnetized flows are not discussed here. Forcing numerical simulations are then necessary, which is out of the scope of this paper. The unbalanced case has not been addressed in this paper. It is also an important issue not only from a theoretical point of view but also from an observational point of view since the most analyzed astrophysical plasma, the inner solar wind, is mainly made of outwards propagating Alfvén waves. This point is left for future works.

ACKNOWLEDGMENTS

We thank A. Alexakis for useful discussions. This work is supported by INSU/PNST-PCMI programs and CNRS/GdR Dynamo. This work was supported by the ANR Project No. 06-BLAN-0363-01 "HiSpeedPIV." Computation time was provided by IDRIS (CNRS) Grant No. 070597.

[1] T. Tajima and K. Shibata, *Plasma Astrophysics* (Westview Press, Boulder, USA, 2002).
[2] M. L. Goldstein and D. A. Roberts, Phys. Plasmas **6**, 4154 (1999).
[3] S. Galtier, J. Low Temp. Phys. **145**, 59 (2006).
[4] P. S. Iroshnikov, Sov. Astron. **7**, 566 (1964).
[5] R. H. Kraichnan, Phys. Fluids **8**, 1385 (1965).
[6] D. Montgomery and L. Turner, Phys. Fluids **24**, 825 (1981).
[7] J. V. Shebalin, W. H. Matthaeus, and D. Montgomery, J. Plasma Phys. **29**, 525 (1983).
[8] J.-C. Higdon, Astrophys. J. **285**, 109 (1984).
[9] S. Oughton, E. R. Priest, and W. H. Mattaheus, J. Fluid Mech. **280**, 95 (1994).
[10] P. Goldreich and S. Sridhar, Astrophys. J. **438**, 763 (1995).
[11] C. S. Ng and A. Bhattacharjee, Astrophys. J. **465**, 845 (1996).
[12] R. M. Kinney and J. C. McWilliams, Phys. Rev. E **57**, 7111 (1998).
[13] W. H. Matthaeus, S. Oughton, S. Ghosh, and M. Hossain, Phys. Rev. Lett. **81**, 2056 (1998).
[14] S. Galtier, S. V. Nazarenko, A. C. Newell, and A. Pouquet, J. Plasma Phys. **63**, 447 (2000).
[15] J. Cho, A. Lazarian, and E. T. Vischniac, Astrophys. J. **564**, 291 (2002).
[16] S. Galtier, S. V. Nazarenko, A. C. Newell, and A. Pouquet, Astrophys. J. **564**, L49 (2002).
[17] L. J. Milano, W. H. Matthaeus, P. Dmitruk, and D. C. Montgomery, Phys. Plasmas **8**, 2673 (2001).
[18] W.-C. Müller, D. Biskamp, and R. Grappin, Phys. Rev. E **67**, 066302 (2003).
[19] M. K. Verma, Phys. Rep. **401**, 229 (2004).
[20] B. D. G. Chandran, Phys. Rev. Lett. **95**, 265004 (2005).
[21] W.-C. Müller and R. Grappin, Phys. Rev. Lett. **95**, 114502 (2005).
[22] S. Boldyrev, Phys. Rev. Lett. **96**, 115002 (2006).
[23] B. Bigot, S. Galtier, and H. Politano, Phys. Rev. Lett. **100**, 074502 (2008).
[24] T. S. Horbury, in *Plasma Turbulence and Energetic Particles in Astrophysics*, edited by M. Ostrowski and R. Schlickeiser (University of Jagiellonski, Cracow, 1999), p. 115.
[25] S. Dasso, L. J. Milano, W. H. Matthaeus, and C. W. Smith, Astrophys. J. **635**, L181 (2005).
[26] B. G. Elmegreen and J. Scalo, Annu. Rev. Astron. Astrophys. **42**, 211 (2004); J. Scalo and B. G. Elmegreen, *ibid.* **42**, 275 (2004).
[27] S. Galtier, A. Pouquet, and A. Mangeney, Phys. Plasmas **12**, 092310 (2005).
[28] J. Cho and E. T. Vishniac, Astrophys. J. **539**, 273 (2000).
[29] J. Maron and P. Goldreich, Astrophys. J. **554**, 1175 (2001).
[30] D. Shaikh and G. Zank, Astrophys. J. **656**, L17 (2007).
[31] V. E. Zakharov, V. L'vov, and G. E. Falkovich, *Kolmogorov Spectra of Turbulence I: Wave Turbulence* (Springer-Verlag, Berlin, Germany, 1992).
[32] A. C. Newell, S. V. Nazarenko, and L. Biven, Physica D **152-153**, 520 (2001).
[33] S. V. Nazarenko, New J. Phys. **9**, 307 (2007).
[34] J.-C. Perez and S. Boldyrev, Astrophys. J. **672**, L61 (2008).
[35] S. Galtier, H. Politano, and A. Pouquet, J. Plasma Phys. **61**, 507 (1999).
[36] S. Oughton, P. Dmitruk, and W. H. Matthaeus, Phys. Plasmas **11**, 2214 (2004).
[37] L. Smith and F. Waleffe, Phys. Fluids **11**, 1608 (1999).
[38] R. Bruno and V. Carbone, Living Rev. Solar Phys. **2**, 1 (2005).
[39] A. Alexakis, B. Bigot, H. Politano, and S. Galtier, Phys. Rev. E **76**, 056313 (2007).
[40] A. Alexakis, Astrophys. J. **667**, L93 (2007).

[41] J. Mason, F. Cattaneo, and S. Boldyrev, Phys. Rev. Lett. **97**, 255002 (2006).
[42] S. Galtier and B. D. G. Chandran, Phys. Plasmas **13**, 114505 (2006).
[43] H. Politano, A. Pouquet, and V. Carbone, Europhys. Lett. **43**, 516 (1998).
[44] D. Biskamp and E. Schwarz, Phys. Plasmas **8**, 3282 (2001).
[45] B. Bigot, S. Galtier, and H. Politano, Phys. Rev. Lett. **100**, 074502 (2008).